Modeling of CD16, 2B4 and NKG2D stimulation in natural killer cell activation

Sahak Z. Makaryan[a] and Stacey D. Finley[a,b]*

[a]Department of Biomedical Engineering, University of Southern California, Los Angeles, California, United States of America

[b]Mork Family Department of Chemical Engineering and Materials Science, University of Southern California, Los Angeles, California, United States of America

* Corresponding author
Stacey D. Finley
1002 Childs Way, MCB 356
Los Angeles, CA 90089
Phone: 213-740-8788
Email: sfinley@usc.edu

Running title: Modeling NK cell receptor stimulation

Abstract

Natural killer (NK) cells are innate immune effector cells that play an immediate role in host defense. NK cells contain a variety of stimulatory pathways that induce the release of cytotoxic chemicals when activated. Mathematical modeling of such pathways can inform us about the magnitude and kinetics of activation. This, in turn, can provide insight for NK cell-based therapies. To quantitatively understand the differences between three main stimulatory pathways in NK cells (CD16, 2B4 and NKG2D), we developed a mathematical model that mechanistically describes their intracellular signaling dynamics. In particular, the model predicts the dynamics of the phosphorylated receptors, pSFK, pErk, pAkt and pPLCγ, as these species contribute to cell activation. The model was fit to published experimental data and validated with separate experimental measurements. Modeling simulations show that the CD16 pathway exhibits rapid activation kinetics for all species, and co-stimulation of CD16 with either NKG2D or 2B4 induces the greatest magnitude of activation. Moreover, the magnitude of cell activation under co-stimulation is more sensitive to CD16 stimulation than either 2B4 or NKG2D stimulation. Overall, the model predicts CD16 stimulation is more influential in cell activation. These modeling results complement ongoing experimental work that applies CD16 stimulation for therapeutic purposes.

Introduction

Mathematical modeling of signal transduction pathways provides a framework that enables better cell engineering approaches. Indeed, many models have augmented our understanding of biological processes (Bellouquid and CH-Chaoui, 2014; Eftimie et al., 2016; Pappalardo et al., 2012) by generating quantitative detail and actionable insight. As an example, researchers investigating the EGFR pathway in an *in silico* cancer cell model demonstrated that inhibition of multiple upstream processes significantly attenuates signal propagation (Araujo et al., 2005). These findings would later support the use of multi-kinase inhibitors as a potential cancer therapeutic (Gridelli et al., 2007; Zhou, 2012). Despite such advances, a few areas of biology provide new opportunities to be explored by quantitative, engineering-based computational models (Baxter and Hodgkin, 2002). Immunology is one example, and in particular, tumor immunology can benefit from robust computational modeling. Recently, the advent of cancer immunotherapy (Bollino and Webb, 2017; Klingemann, 2005) has engendered a new hope for cancer patients and their families. In fact, immunotherapy is meritoriously considered a breakthrough therapeutic approach in the clinic, especially as an effective treatment for hematological cancers (Gattinoni et al., 2006; Mellman et al., 2011; Rosenberg et al., 2004). Ongoing work is aimed at achieving similar success for solid tumors. Mechanistic models of tumor-immune cell interactions can help identify new strategies and potentially enhance the success rate of immunotherapies against solid tumors.

Natural killer (NK) cells are one of the first immune effector cells to interact with solid tumors (Bryceson and Ljunggren, 2011a, 2011b; Guillerey et al., 2016). Briefly, NK cells recognize host cells via detection of the major histocompatibility complex type-I (MHC-I) molecule. This molecule interacts with inhibitory receptors found on NK cells and inhibits the release of cytotoxic chemicals, preventing NK cells from attacking the body's own cells. In contrast, cancer cells are often observed with a downregulated MHC-I expression profile (Bubeník, 2003; Ramnath et al., 2006) and an upregulated surface expression of tumor-associated antigens (Disis and Cheever, 1996; Nanda and Sercarz, 1995) that bind to stimulatory receptors on NK cells. This combination of changes in cancer cell surface expression results in the cancer cell being eliminated upon contact with NK cells. While this tumor-NK cell interaction selectively eliminates cancer cells with a reduced expression of MHC-I (Bryceson and Ljunggren, 2011a, 2011b), it unfortunately cannot prevent cancer cells with sufficient MHC-I expression from escaping NK cell cytotoxicity (Kwon et al., 2016). In order to effectively suppress cancer cell proliferation, NK cells must be able to kill the cancer cell despite MHC-I expression. This could be accomplished by having a net stimulatory signal even when stimulatory and inhibitory receptors are activated on the NK cell simultaneously. Multiple receptors can contribute to the stimulatory signal, each differentially affecting the magnitude and kinetics of the signaling response. Thus, understanding and controlling their dynamics is difficult to achieve using experimental studies alone, and a theoretical framework of NK cell activation is needed.

Previously, researchers have modeled NK cell activation under different conditions and scenarios. For example, work by Das demonstrates how receptor-ligand interactions for a generic stimulatory receptor impacts NK cell activation using phosphorylated Erk (pErk) as a readout (Das, 2010). In another example, Mesecke and colleagues determined that the physical association of Src family kinases (SFK) with a stimulatory receptor is essential for NK cells to promote a cytotoxic response (Mesecke et al., 2011). In both cases, the models simulate an individual stimulatory receptor, which does not account for the fact that NK cells express a repertoire of stimulatory receptors. In fact, there is currently no quantitative study that compares the effects of multiple stimulatory pathways on NK cell activation. Such a study can help identify unique signaling properties inherent within the pathways and provide rationale for designing NK cell activation-based immunotherapies. Here, we present a new computational model that goes beyond previous models (Das, 2010; Mesecke et al., 2011) by including more molecular detail, and by comparing multiple pathways that have distinct signaling features and are implicated in unique NK cell-mediated processes.

The stimulatory pathways explored in this study are CD16, 2B4 and NKG2D, due to their strong impact on NK cell activation. These pathways differ in both the context and mechanism of NK cell activation (Chen et al., 2004; Gilfillan et al., 2002; Theorell et al., 2014). CD16 is an Fc receptor that binds to the constant region of antibodies. This emphasizes CD16's activation in antibody-dependent cell-mediated cytotoxicity (ADCC). Its cytoplasmic domain is associated with CD3ζ, which contains immunoreceptor tyrosine-based activation motifs (ITAM). 2B4 is part of the signaling lymphocytic activation molecule (SLAM) family of receptors, and its cytoplasmic tail contains four immunoreceptor tyrosine-based switch motifs (ITSM). The ligand for 2B4, CD48, is expressed by cells of hematopoietic origin. This suggests 2B4 may play a role in regulating hematopoietic processes. NKG2D belongs to the family of C-type lectin-like receptors and associates with the adaptor protein DAP10, which has an activation motif that is similar to the CD28 T cell co-receptor. NKG2D binds to ligands typically expressed by cells that have undergone transformation (e.g., induced-self antigen expression), which implicates this receptor in the elimination of tumors.

Ligand binding to CD16, 2B4 and NKG2D initiates intracellular signaling through multiple pathways. The PI3K-Akt, SLP76-Vav-Erk and PLCγ networks are all activated upon CD16, 2B4 and NKG2D stimulation (Long et al., 2013). In NK cell biology, the PI3K-Akt pathway promotes cell survival, while Erk activation leads to cell proliferation. SLP76 and Vav activation are necessary for actin remodeling, a prerequisite for the formation of the immunological synapse and degranulation of cytotoxic chemicals. Lastly, PLCγ activation induces the release of intracellular calcium ions, which subsequently activates the cell. The integration of these intracellular reactions is necessary to activate NK cells. Many of these downstream reactions are common between the pathways with only subtle differences. Specifically, 2B4 leads to PI3K activation, but does not induce Akt phosphorylation (Kim and Long, 2012; Kwon and Kim, 2012). Additionally, 2B4 and NKG2D specifically lead to phosphorylation of the Y113 and Y128 sites on SLP76, respectively, while CD16 induces activation of both sites (Kim and Long, 2012). Also, CD16 induces ZAP70 and LAT activation, while 2B4 and NKG2D do not.

In the present study, we characterize and compare the dynamics of multiple stimulatory pathways with respect to their magnitude and kinetics of activation. We developed a detailed mechanistic model of the intracellular signaling pathways activated by CD16, 2B4 and NKG2D. The model is applied to predict the dynamics of key signaling species in the pathways, revealing qualitative and quantitative differences between the signaling promoted by each receptor. Overall, the model is a quantitative framework that captures NK cell signaling mediated by stimulatory receptors. Such a framework is needed to further investigate NK cell biology and its immunotherapy applications.

Results

Model calibration

We generated a mathematical model of NK cell signaling that includes three main pathways: CD16, 2B4 and NKG2D. When these receptors are stimulated, they activate the cell via cascades of phosphorylation reactions (**Figure 1**): activation of the Src family kinases (SFK), facilitated by the ligand-bound phosphorylated receptors, catalyzes the activation of the PI3K-Akt, SLP76-Vav-Erk, and PLCγ pathways. The accumulation of phosphorylated species in these pathways ultimately leads to cell activation. We simulated these reactions in the form of ordinary differential equations (ODEs) using established Michaelis-Menten kinetics and the law of mass-action for enzymatic and binding reactions, respectively.

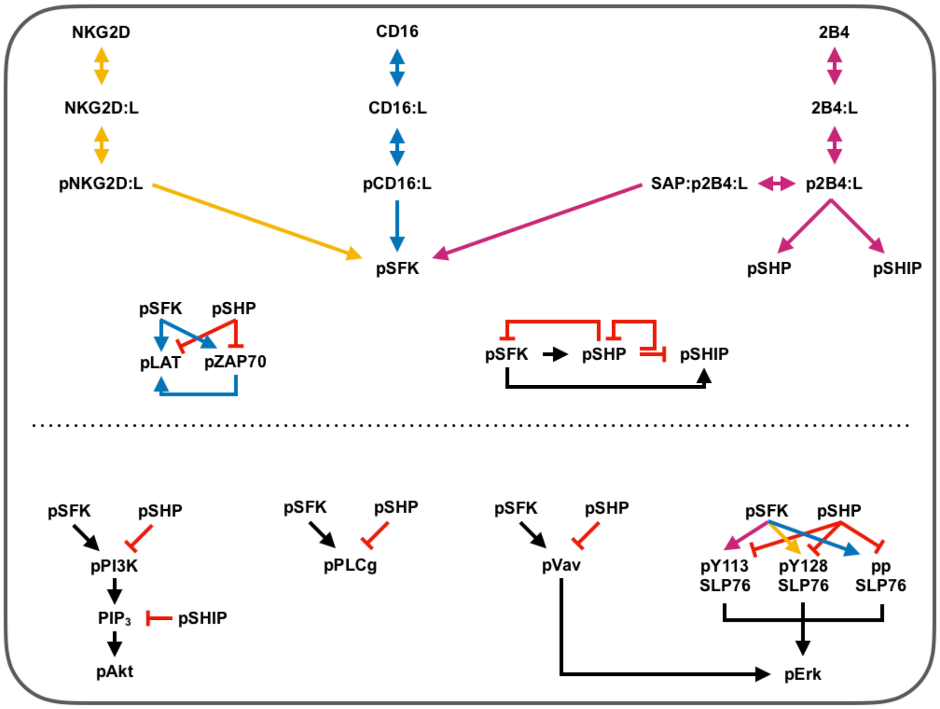
NKG2D
NKG2D:L
pNKG2D:L
CD16
CD16:L
pCD16:L
pSFK
2B4
2B4:L
SAP:p2B4:L
p2B4:L
pSHP
pSHIP
pSFK
pSHP
pLAT
pZAP70
pSFK
pSHP
pSHIP
pSFK
pSHP
pPI3K
PIP₃
pSHIP
pAkt
pSFK
pSHP
pPLCg
pSFK
pSHP
pVav
pSFK
pSHP
pY113 SLP76
pY128 SLP76
pp SLP76
pErk

Figure 1. Model schematic. Reaction network for three stimulatory receptors expressed on the surface of NK cells: CD16, 2B4 and NKG2D. These receptors promote signaling species that mediate NK cell activation: SFK, Erk, Akt and PLCγ. Arrows indicate stimulation while red crossbars indicate inhibition. Orange arrows are specific to the NKG2D pathway; blue, CD16 pathway; purple, 2B4 pathway; black, all pathways. The dashed lines separate the upstream reactions from the downstream reactions.

The model was calibrated to immunoblot data (Billadeau et al., 2003; Kim and Long, 2012; Kim et al., 2010; Ting et al., 1992). We quantified the temporal change in signal intensity of protein bands from images of immunoblot experiments using ImageJ (NIH). Specifically, we used the normalized levels of phosphorylated species: pSFK, pZAP70, pLAT, ppSLP76, pPLCγ, pVav, pErk, pAkt, and SLP76 phosphorylated at pY113 and pY128. The model also predicts the dynamics of these species ("model outputs"). We estimated the parameter values using an iterative approach combining sensitivity analysis and model optimization. We first applied a global sensitivity analysis to identify the influential parameters in the model. We assumed that most of the variability between the three pathways would be found in the upstream reactions (e.g., receptor-ligand interactions), since many of the downstream reactions (e.g., PLCγ and PI3K phosphorylation) are common in all the pathways. Thus, we performed a sensitivity analysis (Marino et al., 2008) by estimating how much the model outputs vary when the kinetic parameters of the upstream reactions ("model inputs") are varied. The results of our analysis identified 56 parameters that significantly affect the model outputs (**Figure S1**).

We then performed parameter estimation using the particle swarm optimization (PSO) method (Kennedy, 2011; Shi, 2004; Venter and Sobieszczanski-Sobieski, 2003). PSO searches the parameter-space for solutions that minimize the error between the model predictions and the experimental data. The algorithm was executed 50 times with random initial guesses, and the sum of squared errors (SSE) between the model predictions and experimental data was used to determine the goodness-of-fit. The estimated parameter values from the fitting procedure are shown in **Figure S2**. The kinetic parameters that varied over one order of magnitude, based on Tukey's box-and-whisker plot (Chambers et al., 1983), were kept constant at their median values, while the parameters that varied in a tighter range were selected for the next round of fitting using PSO fifty times. This iterative approach reduced the number of parameters to fit from 56 to 15 to 13 in successive rounds (**Figure S2, A-D**). The final fitting procedure resulted in a mean SSE value of 2.45 $\pm$ 0.02. The results from model calibration (**Figure 2**) show that the model predictions quantitatively match the experimental data for mono-stimulation of CD16 (blue lines in **Figure 2, A-C and E-G**), 2B4 (purple lines in **Figure 2, E-H**), and NKG2D (orange lines in **Figure 2, D-H**). Overall, the model predictions reproduce the experimental data.

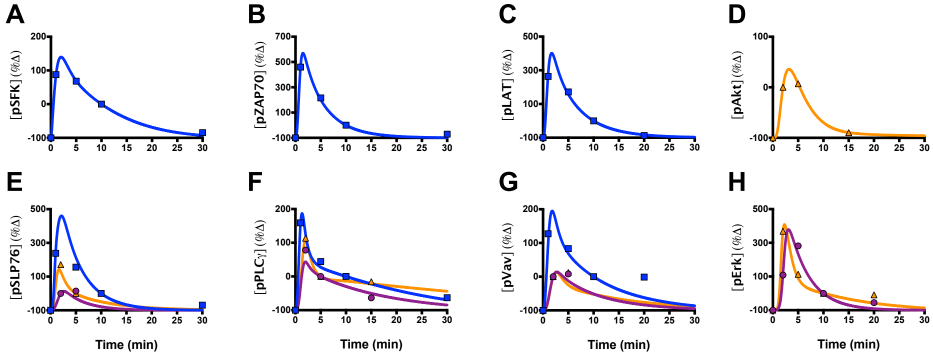

Figure 2. Model calibration. The model was fit to experimental data for (A) pSFK, (B) pZAP70, (C) pLAT, (D) pAkt, (E) pSLP76, (F) pPLCγ, (G) pVav and (H) pErk. Blue: CD16 pathway. Purple: 2B4 pathway. Orange: NKG2D pathway. Model predictions: solid lines. Experimental data: squares, CD16 stimulation; circles, 2B4 stimulation; triangles, NKG2D stimulation.

Model validation

Our mathematical model of NK cell signaling can recapitulate the effects of a variety of perturbations to the system. Model validation ensures that we have constructed a robust framework that can be used to analyze the network structure and extract meaningful insight about the pathways. To validate the model, we compared the model predictions to separate experimental data not used during training. Specifically, we extracted measurements of intracellular species when NK cells were simultaneously stimulated by multiple receptors or in the presence of molecular perturbations (e.g., RNA interference, kinase inhibitors, species knockdown) (Dong et al., 2012; Kim et al., 2010; Kwon et al., 2015, 2016; Pérez-Quintero et al., 2014). RNA interference and species knockdown experiments were simulated by decreasing the initial concentration of the species of interest in our model, and kinase inhibitors were simulated via decreasing the reaction rates of interest.

The results from model validation are shown in **Figure 3**. The model captures the co-stimulation of 2B4 and NKG2D without inhibition (**Figure 3, A-D**) and in the presence of various perturbations that inhibit signaling (**Figure 3, F-H**). The model captures the time evolution of pVav in the presence of SAP knockdown under 2B4 mono-stimulation (**Figure 3, E**). Overall, the mean SSE value between the model predictions and the validation data was 12.23 $\pm$ 0.06. Altogether, the model accurately predicts the effects of a variety of perturbations. This validated model allows us to derive meaningful comparisons between the pathways.

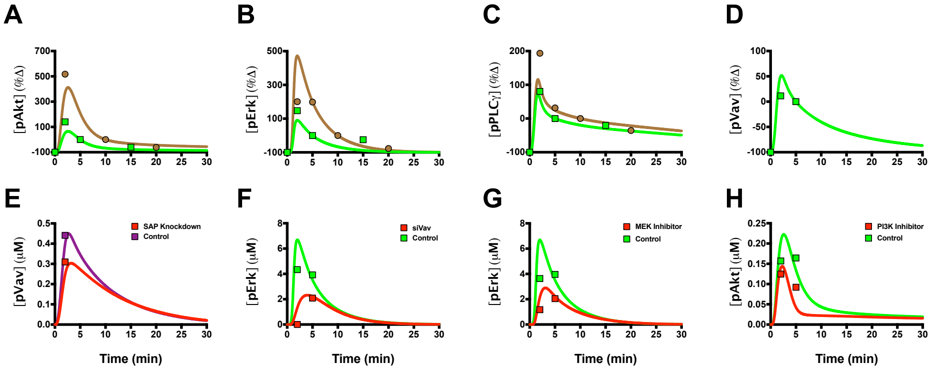

Figure 3. Model validation. The model was validated against separate experimental data, including the concentrations of: (A) pAkt, (B) pErk, (C) pPLCγ and (D) pVav over time via co-stimulation of 2B4 and NKG2D. The model was validated against data that incorporates signal-inhibiting perturbations: (E) pVav over time with SAP knockdown via 2B4 mono-stimulation, pErk over time with (F) siVav or (G) MEK inhibitor via 2B4 and NKG2D co-stimulation; (H) pAkt over time with PI3K inhibitor via 2B4 and NKG2D co-stimulation. Model predictions: solid lines. Experimental data: circles and squares. For (A) – (D), green and brown data indicate independent experimental studies.

Individual differences in signaling dynamics

Using the validated model, we compared the dynamics between the three pathways. Each receptor was stimulated with $6.67{\times}10^{-2}\mu M$ of its cognate ligand, mimicking experimental studies (Billadeau et al., 2003; Kim and Long, 2012; Kim et al., 2010; Ting et al., 1992). Here, we focus on the dynamics of phosphorylated SFK, PLCγ, Erk, Akt and the activated receptors (pSFK, pPLCγ, pErk, pAkt and pReceptor, respectively) as readouts for cell activation. We characterize the magnitude of these species' activation by examining particular aspects of their concentration profiles (**Figure 4, A**). A comparison of the time evolution of the activated receptors (**Figure 4, A**) highlights a key difference in the kinetics of activation between the pathways. Specifically, the concentration pCD16 reaches that of total ligand very quickly (within ~ 1 second), while p2B4 and pNKG2D never become fully saturated with ligand. Collectively, these results emphasize the difference in the timescale of the signaling response between CD16 and the other two receptors: pCD16 arrives at maximal ligand concentration almost instantaneously while p2B4 and pNKG2D never reach maximal ligand concentration.

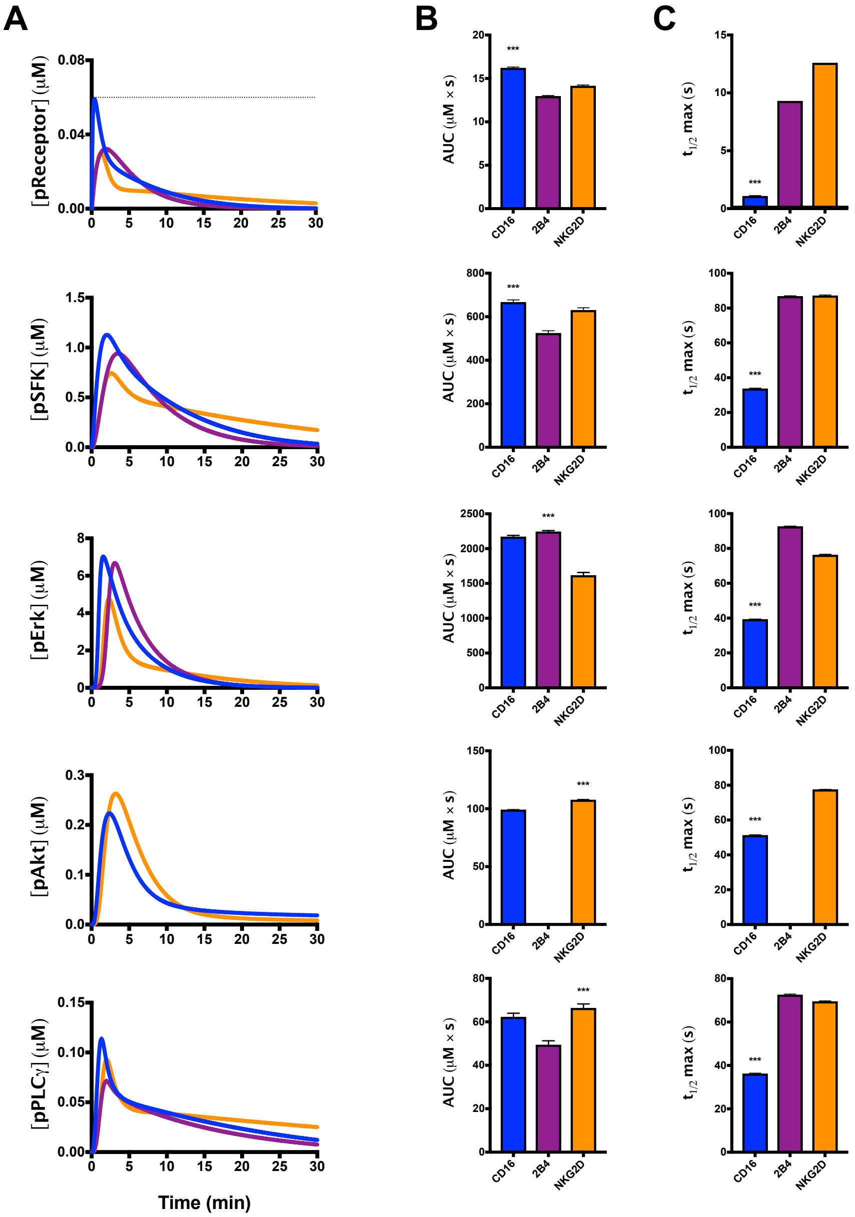

Figure 4. Characteristic signaling differences. (A) Concentration profiles for activation-influencing species: pReceptor, pSFK, pErk, pAkt, and pPLCγ. (B) Magnitude of activation for the corresponding species in panel A via AUC analysis. (C) Time to reach half-maximal concentration for the corresponding species in panel A. Blue: CD16 pathway. Purple: 2B4 pathway. Orange: NKG2D pathway. Asterisks signify the highest AUC or lowest $t_{1/2}\,max$ based on t-test $(p < 0.001)$.

We quantified the area under the curve (AUC), which is the time-averaged activation level (**Figure 4, B**). The magnitude of activation for the activated receptors, characterized by the AUC, demonstrates there is more pCD16 than p2B4 or pNKG2D in the system. CD16 induces greater activation of pSFK compared to stimulation of 2B4 or NKG2D individually. The AUC of pPLCγ and pAkt are greater under NKG2D stimulation, whereas 2B4 stimulation induces a greater activation of pErk. Thus, the receptors have differential effects on the various intracellular signaling pathways.

We also calculated the time required for each species to reach its half-maximal concentration ($t_{1/2}\ \max$) (**Figure 4, C**). Based on this characteristic, the model predicts that there is a clear difference in the time required for the phosphorylated receptors to reach half of the total ligand concentration (**Figure 4, C**), where $t_{1/2}\ \max$ for CD16 is much lower than 2B4 and NKG2D. In fact, CD16 stimulation produces the lowest $t_{1/2}\ \max$ value for all species compared to 2B4 or NKG2D mono-stimulation. Thus, overall, CD16 stimulation leads to a faster activation for all species.

`Taken together, the predicted dynamics of the receptors and the signaling species show that CD16 induces a rapid activation in NK cells. We next investigate whether this is an inherent property of the CD16 pathway or if it is due to other characteristics of the signaling network.

Inherent properties of the pathways

Analysis of the rate of change of the species' concentrations provides insight into the duration and strength of stimulation and differences in the kinetics of activation between the pathways. We employed geometric analyses (Heinrich et al., 2002) of the time-series plots of the derivatives of the species' concentrations. To classify and compare the activation kinetics between the pathways, we focused our analyses on the time period during which the species' concentration is increasing (i.e., $\frac{d}{dt} > 0$) (**Figure 5, A**). Two quantitative descriptors, signal duration (**Figure 5, B**) and signal strength (**Figure 5, C**), categorize the pathways' inherent activation profile. Briefly, signal duration is a measure of the average length of time the species' rate of change is positive, and signal strength is the average intensity of the species' rate of change during the same interval (see Methods for more detail).

For all of the signaling species, the CD16 pathway has the shortest duration of activation (**Figure 5, B**) but is significantly stronger (**Figure 5, C**) compared to the activation that occurs when 2B4 or NKG2D is stimulated. The opposite holds true for the 2B4 pathway. That is, 2B4 stimulation produces a more sustained signal, but with a lower signal strength. The signal duration and strength upon NKG2D stimulation are intermediate between that of CD16 and 2B4. We observe the same trend when it comes to the activated receptors (**Figure 5, A-C**, *top panel*). The signal duration of pCD16 is short ($\sim$ 10 s) compared to p2B4, whose signal duration is significantly longer ($\sim$ 70 s). The signal duration of pNKG2D is intermediate ($\sim$ 40 s). The signal strength of the activated receptors has the opposite trend: pCD16 $\gg$ pNKG2D $>$ p2B4. In summary, the CD16 pathway exhibits strong but transient activation kinetics. On the other end of the spectrum, the 2B4 pathway displays weak but sustained activation kinetics. Thus, analyzing the time derivatives of the species' concentrations provides a way to classify the timescale over which the species are activated within each pathway.

The predicted differences between the pathways' activation kinetics can be explained by examining the estimated parameters. Specifically, we examine the dissociation constants and the enzyme catalytic efficiency. The dissociation constant, K_D, is defined as the ratio of the dissociation rate constant to the association rate constant: $K_D = \frac{k_{off}}{k_{on}}$. This quantity measures the affinity between two species, with a smaller K_D signifying a tighter bond between the species. During model fitting, we fixed k_{on} and fit k_{off} for each receptor-ligand interaction (see Methods). The estimated parameter values indicate that CD16 has a greater affinity for its ligand (**Figure 6, A**). Additionally, the initial concentration value of the CD16 receptor is reported to be two orders of magnitude higher than 2B4 and NKG2D ($38.26\ \mu M$ compared to 0.35 and $0.30\ \mu M$ for 2B4 and NKG2D, respectively) (Kim et al., 2014). Since the law of mass action states that the rate of a reaction is proportional to the concentration of its reactants, we reduced the initial concentration of CD16 by two orders of magnitude to determine if CD16's rapid activation kinetics is primarily a result of its large initial value (**Figures S4** and **S5**). The dynamics of the downstream species remain unchanged when comparing **Figures 4** and **5** to **Figures S4** and **S5**. However, pCD16 does not become fully saturated when its initial value is decreased by 100-fold (**Figure S4, A,** *top panel*). While $t_{1/2}\max$ for pCD16 does increase when its initial value is reduced by 100-fold, it is still lower than p2B4 or NKG2D (**Figure S4, C,** *top panel*). Thus, it is CD16's strong affinity for its ligand that explains the rapid activation kinetics observed under CD16 stimulation (**Figure 4, C**).

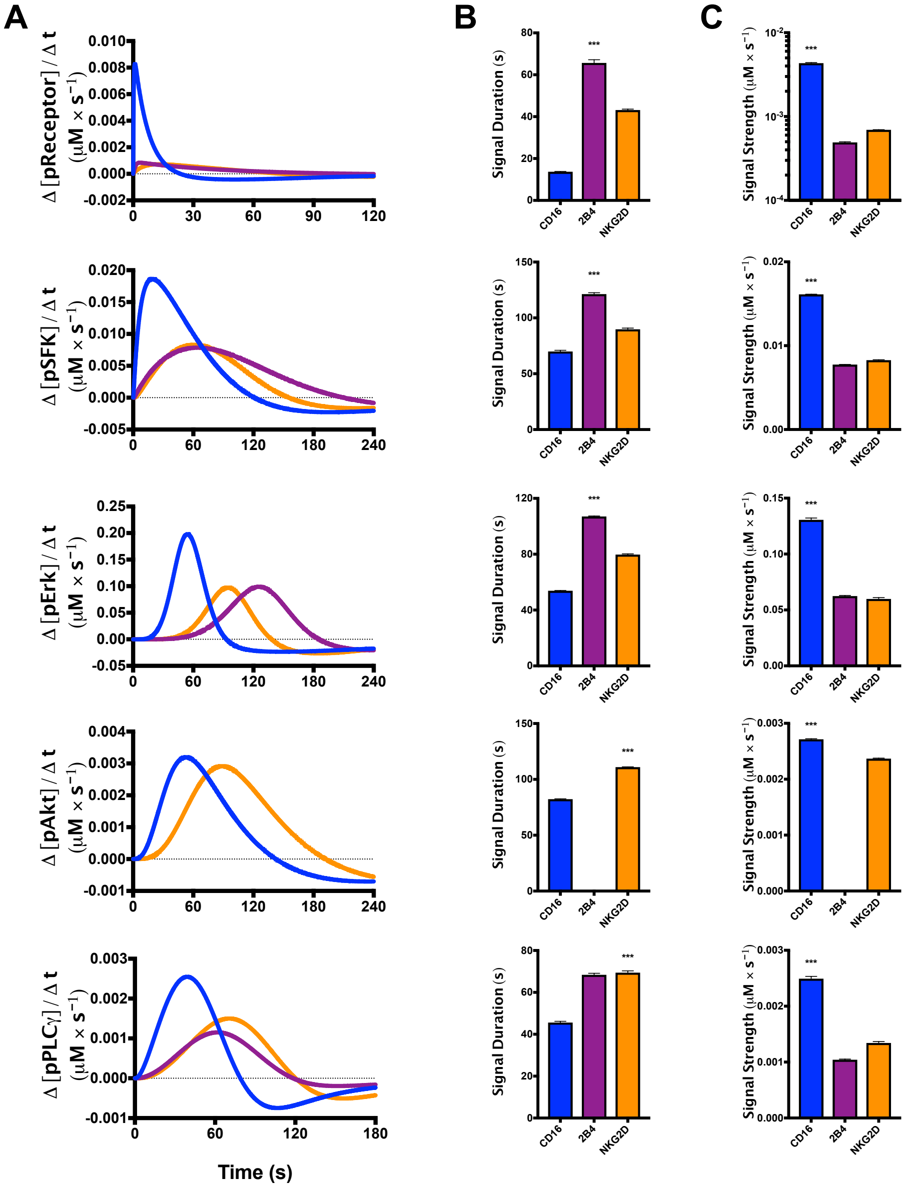

Figure 5. Kinetic analysis of species activation. (A) Time derivatives of the concentration profiles for activation-influencing species: pReceptor, pSFK, pErk, pAkt, and pPLCγ. (B) The calculated signal duration for the corresponding species in panel A. (C) The signal strength for the corresponding species in panel A. Blue: CD16 pathway. Purple: 2B4 pathway. Orange: NKG2D pathway. Asterisks signify the highest signal duration or signal strength based on *t*-test ($p < 0.001$).

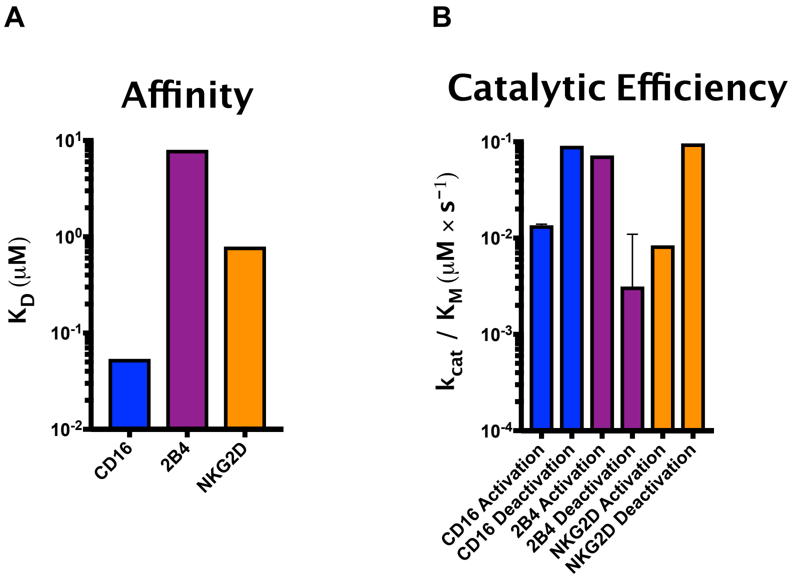

Figure 6. Comparison of estimated parameter values for pathway activation. (A) The estimated dissociation constant (K_D) between each receptor and its ligand, and (B) catalytic efficiency $(\frac{k_{cat}}{K_M})$ for receptor activation and deactivation. Blue: CD16 pathway. Purple: 2B4 pathway. Orange: NKG2D pathway.

We also investigated the predicted catalytic efficiency for receptor activation and deactivation to gather further insight of the system. The catalytic efficiency is expressed as the ratio of the turnover rate to the Michaelis-Menten constant: $\frac{k_{cat}}{K_M}$. The parameter estimation indicates that the activation and deactivation of CD16 and NKG2D occur with comparable catalytic efficiencies (**Figure 6, B**). For these receptors, deactivation occurs more efficiently than activation. In contrast, activation of 2B4 is much more efficient than its deactivation. This property explains the relatively long signal duration of the species (**Figure 5, B**) under 2B4 stimulation. Taken together, the analyses of the species' time derivatives and the estimated parameter values help explain CD16's strong activation profile and 2B4's sustained signal.

Effects of combinatorial stimulation

Mono-stimulation, or co-stimulation of the receptors in pairwise combinations, demonstrates CD16's significance in NK cell activation *in silico*. We increased the ligand concentration for each receptor by two orders of magnitude from the baseline value of $6.67\times10^{-2}\,\mu M$ to better understand how the downstream species are affected by ligand availability. We calculated the AUC for pSFK (**Figure 7, A**), pErk (**Figure 7, B**), pAkt (**Figure 7, C**) and pPLCγ (**Figure 7, D**) after 30 minutes of ligand stimulation. The magnitude of activation for pSFK and pAkt is more sensitive to CD16 stimulation, as compared to 2B4 or NKG2D (**Figure 7, A** and **C**). Phosphorylated Erk activation levels are comparable under CD16 and 2B4 stimulation, but both induce greater activation than NKG2D stimulation (**Figure 7, B**). Activation levels of pPLCγ are particularly sensitive to the stimulation of CD16 and 2B4, and this species has a biphasic response under CD16 stimulation (**Figure 7, D**). We observe a similar biphasic response for pSFK and pPLCγ activation under the 2B4 pathway (**Figure 7, A** and **D**). This behavior is explained in detail below.

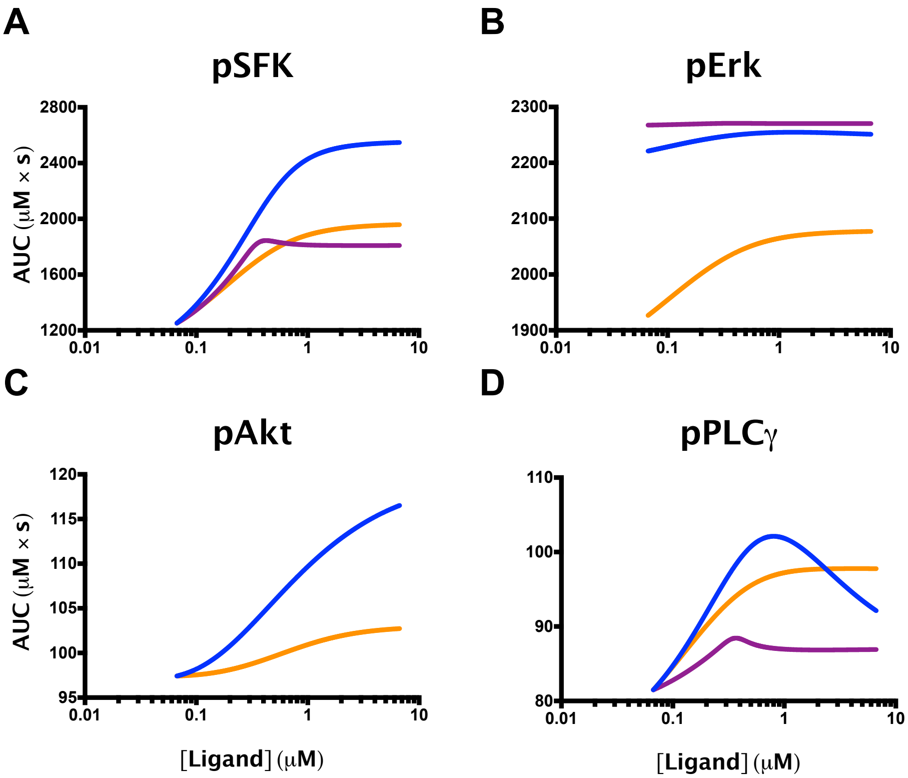

Figure 7. Mono-stimulation of receptors with various ligand concentrations. The AUC of (A) pSFK, (B) pErk, (C) pAkt and (D) pPLCγ was calculated after 30 minutes of ligand stimulation. For each panel, the ligand concentrations were varied by two orders of magnitude from baseline $(6.67\times10^{-2}\mu M)$. Blue, mono-stimulation of CD16; Purple, mono-stimulation of 2B4; Orange, mono-stimulation of NKG2D.

For the co-stimulation studies, we analyzed the AUC of pSFK (**Figure 8, A**), pErk (**Figure 8, B**), pAkt (**Figure 8, C**) and pPLCγ (**Figure 8, D**) as a readout for the magnitude of cell activation. We again increased the ligand concentrations up to two orders of magnitude from the baseline value. Interestingly, the AUC for all species increases when CD16 is co-stimulated with either 2B4 or NKG2D, compared to mono-stimulation (**Figure 7**) and compared to co-stimulation of 2B4 and NKG2D. Indeed, comparison of column one (2B4 + NKG2D) with columns two or three (CD16 + 2B4 or CD16 + NKG2D) in **Figure 8**, shows that CD16 stimulation increases the activation of each downstream species (**Figure 8, A-D**). Additionally, there is a more significant change in the AUC for CD16 + 2B4 and CD16 + NKG2D combinations in the horizontal direction (increasing CD16 concentration). That is, varying CD16 has a greater effect on the concentrations of the activated signaling species compared to 2B4 or NKG2D. Collectively, the model predicts that: (1) the activation of pSFK, pErk, pAkt and pPLCγ is greatest when CD16 is co-stimulated with either 2B4 or NKG2D, and (2) the activation of each of the activated signaling species is more sensitive to CD16 stimulation.

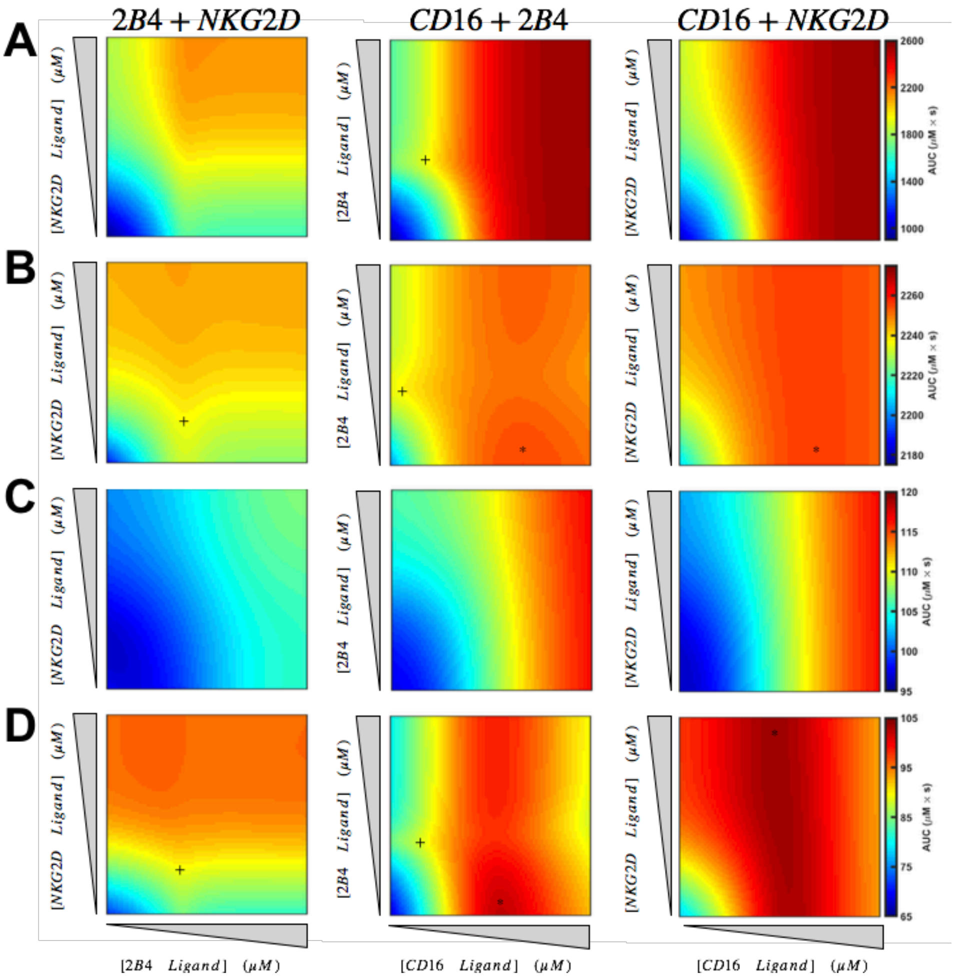

Figure 8. Pairwise stimulation of receptors with various ligand concentrations. The AUC of (A) pSFK, (B) pErk, (C) pAkt and (D) pPLCγ as a function of ligand concentration. For each panel, the concentration of ligands was varied by two orders of magnitude from baseline $(6.67\times 10^{-2}\mu M)$. Left column, co-stimulation of 2B4 and NKG2D; middle column, co-stimulation of CD16 and 2B4; right column, co-stimulation of CD16 and NKG2D.

The model also predicts that under some conditions, mono-or co-stimulation promotes a biphasic response. Specifically, for mono-stimulation, the AUC for pSFK peaks at intermediate 2B4 concentrations. Similarly, the AUC for pPLCγ is highest for intermediate concentrations of CD16. For co-stimulation, the highest AUC values for pErk and pPLCγ occur at intermediate CD16 ligand concentrations (exemplary cases are denoted by "$*$" in **Figure 8**), rather than exhibiting a monotonic increase as the CD16 ligand concentration increases. 2B4 can also promote a biphasic response for SFK, Erk, and PLCγ (exemplary cases are denoted by "$+$" in **Figure 8**) under co-stimulatory conditions, although to a lesser degree. The model indicates that the biphasic responses are due to negative feedback. In the CD16 pathway, increasing CD16 ligand concentration increases the activation of the phosphatase SHP via an increase in pSFK activation (Galandrini et al., 2002) in a feedforward manner (**Figure 1**). This increase in phosphatase activation can then inhibit many downstream species. In the 2B4 pathway, similarly, increasing 2B4 ligand concentration can lead to recruitment and activation of SHP and SHIP (Aoukaty and Tan, 2002; Dong et al., 2012; Pérez-Quintero et al., 2014). Upon 2B4 stimulation, p2B4 can immediately recruit and activate these phosphatases. The adaptor molecule SAP must bind to p2B4 in order to promote pSFK activation instead of activating the phosphatases (**Figure 1**). SAP is essential in characterizing 2B4 as a stimulatory receptor, since its absence changes the nature of 2B4 signaling from stimulatory to inhibitory (Aoukaty and Tan, 2002; Dong et al., 2012; Pérez-Quintero et al., 2014). However, increasing 2B4 ligand concentration such that ligated 2B4 receptors overwhelm the amount of SAP in the cell shifts the balance in favor of activating SHP and SHIP rather than SFK. Thus, given the mechanistic detail of our model, we can explain the non-intuitive predictions and quantitative details regarding NK cell signaling dynamics.

Discussion

In this study, we constructed a molecularly-detailed, validated mathematical model of signaling pathways that mediate NK cell activation. We aimed to use the model to mechanistically understand the differences between different stimulatory pathways and how these pathways influence the NK cell activation. CD16 activates all the species much more rapidly than 2B4 or NKG2D. Analyses of the time derivatives of the species' concentrations and the estimated parameter values reveal the qualitative nature of activation for each pathway. CD16 induces strong but transient kinetics, whereas 2B4 produces a weak but sustained signal. NKG2D falls within in the middle of this spectrum. The *in silico* studies of receptor co-stimulation revealed that the combinations involving CD16 stimulation were more effective in increasing the AUC for all species, and that the AUC values for all species were more sensitive to CD16 ligand concentration than to 2B4 or NKG2D ligand concentration.

The work presented in this study provides quantitative mechanistic insight on CD16's significance as a stimulatory receptor when compared with 2B4 and NKG2D. Although experimental studies (Kim and Long, 2012) have found that CD16 plays a dominant role in NK cell stimulatory signaling compared to other receptors, little effort has been devoted towards mechanistically understanding the differences between pathways or how combinations of the pathways affect activation in NK cells. Our mathematical model helps to fill this void and provides a deeper appreciation as to why CD16 is a potent receptor for activation. Importantly, the model provides a quantitative explanation for CD16's greater effect on signaling that is difficult to obtain experimentally.

Researchers in recent years have designed combinatorial chimeric antigen receptors (CARs) for NK cells that include intracellular signaling domains of CD16 (CD3ζ), 2B4 and NKG2D for anti-tumor therapy (Altvater et al., 2009; Li et al., 2018). With the insight generated by our model, it is not unexpected that CARs comprised of CD16, 2B4 and NKG2D signaling domains together outperformed CARs with a single domain alone. Moreover, pre-clinical work in CAR-NK cell immunotherapies (Glienke et al., 2015; Romanski et al., 2016) predominantly include CD16's intracellular domain in combination with other co-stimulatory domains (e.g., 4-1BB or DAP10). Through continued success in the pre-clinical stage, a few CAR-NK cell immunotherapies have entered clinical trials as a potential therapeutics for cancer patients. Additionally, antibody engineering methods (Romain et al., 2014) for the CD16 receptor have shown potential in inducing "serial" killing of multiple target cells by NK cells. Overall, the kinetic analyses carried out in this study provides a quantitative explanation to complement the conclusions of multiple independent studies, with the overarching finding that CD16 (along with its components) is a potent stimulator of NK cell activation.

We acknowledge some limitations and assumptions that may affect the model predictions. Although multiple sites of phosphorylation and dephosphorylation can exist for each species, we have not included this level of detail in the model. Accounting for multi-site phosphorylation and dephosphorylation reactions would increase the specificity of our model, but at the expense of model simplicity. Since we are primarily interested in understanding and comparing the dynamics between multiple receptor pathways and how they activate the NK cell, we sought to simplify the pathways in order to effectively compare them. In the future, we can consider the specific phosphorylation sites and their importance in particular aspects of NK cell activation. Additionally, the model was trained to normalized experimental data, which could potentially cause scaling issues. The initial conditions were derived from literature when available (Bar-Even et al., 2011; Kim et al., 2014; Northrup and Erickson, 1992; Schlosshauer and Baker); however, we expect that these values may differ based on the specific NK cell line or the donor for primary NK cells. Future research can address these limitations while also building upon the work presented here.

Despite these limitations, our mathematical model is relevant for understanding and guiding the development of NK cell-based therapies. Kinetic analyses can aid in the design of engineered receptors, such as CARs, by predicting which combinations of signaling domains activate the NK cells and induce optimal killing of target cells. Questions within tumor immunology, in particular tumor and NK cell dynamics, can be studied by integrating our kinetic model of activation with a cell-based model. Furthermore, incorporating inhibitory pathways along with the stimulatory pathways modeled here can help explain how tumor cells escape NK cell cytotoxicity by engaging with NK cell inhibitory receptors. Since the model predicts that the CD16 receptor is the more potent inducer of activation, it can be inferred that antibody-coated target cells stimulate NK cell activation at a greater rate and magnitude. Future research can address this model prediction and provide more empirical motivation for CD16-based NK cell immunotherapies. In summary, our work delineates the differences between multiple stimulatory pathways involved in NK cell activation and provides detailed mechanistic insight that helps explain experimental observations. The model can be utilized as a framework for researchers interested in NK cell cytotoxicity and its applications in immunotherapy.

Methods:

Model construction

The model was constructed using BioNetGen (Harris et al., 2016), and all simulations and calculations were subsequently performed in MATLAB (MathWorks). The law of mass action and Michaelis-Menten kinetics were used to describe binding interactions and enzymatic reactions, respectively. The model contains 138 kinetic parameters and 42 species, including the three NK receptors CD16, 2B4 and NKG2D. Each receptor binds to its ligand and forms a receptor-ligand complex that allows the receptor to become phosphorylated by basally active Src family kinases (SFK). Then, the ligand-bound phosphorylated receptor, serves as the catalyst for activating SFK from a basally active state (SFK) towards a fully active state (pSFK). We carefully distinguish the two forms with respect to activity by allowing the basally active form to only phosphorylate the ligand-bound receptor and the fully active form to phosphorylate only downstream species (Mesecke et al., 2011). This ensures the activated receptor is the driving force for the signaling cascade; otherwise, SFK can sufficiently activate the downstream species in the absence of a signal, which is not biologically reasonable.

Fully active SFK mediates the phosphorylation (activation) of a number of downstream signaling species, including LAT, ZAP70, PI3K, PLCγ, Vav and SLP76. Phopshorylated ZAP70 also promotes activation of LAT. Phosphorylated PLCγ promotes the formation of IP3, by hydrolyzing PIP_2, thereby causing the release of intracellular calcium ions. However, we focus on the activation of pPLCγ as a readout for calcium release, as have many experimental and computational studies (Das, 2010; Kim and Long, 2012; Kim et al., 2010; Kwon and Kim, 2012;

Mesecke et al., 2011). Phosphorylated PI3K promotes the phosphorylation of PIP_2 to form PIP_3. Additionally, there is reciprocal feedback between pSFK and the phosphatases SHP and SHIP. The inclusion of inhibitory species, SHP and SHIP, in our NK cell activation model serves to provide negative feedback onto the system. Tyrosine kinases have been observed to phosphorylate and activate SHP and SHIP *in vitro* (Giuriato et al., 1997). Moreover, when a chemically-fixed phospho-tyrosine mimetic is incorporated on SHP, it not only removes the intramolecular basal inhibition but also increases its catalytic activity (Szewczuk et al., 2009). Therefore, we assumed that pSFK can phosphorylate and activate SHP, albeit in a cell stimulatory context.

We focus on the downstream species Erk and Akt. The catalyst for Akt phosphorylation is PIP_3. The catalysts for Erk phosphorylation are the phosphorylated forms of SLP76 as well as the phosphorylated form of Vav. These species are upstream components to the MAPK pathway (Das, 2010; Mesecke et al., 2011). Initial concentration values of the species in our system were extracted from scientific literature (Bar-Even et al., 2011; Kim et al., 2014; Northrup and Erickson, 1992; Schlosshauer and Baker). We simulate the dynamics of signaling network for 30 minutes, to focus on the initial stimulus. Given this time scale, we assume that the synthesis of species is negligible compared to phosphorylation and dephosphorylation reactions (Das, 2010; Mesecke et al., 2011). Lastly, we included a non-specific degradation reaction of the phosphorylated species in the system to account for degradation, dilution and disappearance of the active species, as observed in experimental measurements (Billadeau et al., 2003; Dong et al., 2012; Kim and Long, 2012; Kim et al., 2010; Ting et al., 1992).

Data collection and processing

Immunoblot images from published experimental data were analyzed and processed using an image processing software (ImageJ). In total, the model was trained to 60 data points across ten different species, with a minimum of three data points for a single species. Additionally, the model was validated against 43 data points. The signal intensity ($Q_{p\boldsymbol{X}_j}$) of a given phosphorylated species ($p\boldsymbol{X}$) at the jth time point is calculated as:

$$Q_{p\boldsymbol{X}_j} = \frac{SI_{p\boldsymbol{X}_j}}{SI_{Control_j}}$$

where $SI_{p\boldsymbol{X}_j}$ and $SI_{Control_j}$ are the signal intensity values (obtained from ImageJ) of the phosphorylated species and a loading control, respectively, at the jth time point. Furthermore, the signal intensity ($Q_{p\boldsymbol{X}}$) was normalized to a single (reference) time point by calculating the percent change ($\%\Delta_{p\boldsymbol{X}}$) as follows:

$$\%\Delta_{p\boldsymbol{X}_j} = \frac{Q_{p\boldsymbol{X}_j} - Q_{p\boldsymbol{X}_{ref}}}{Q_{p\boldsymbol{X}_{ref}}} \times 100\%$$

Sensitivity analysis

The extended Fourier Amplitude Sensitivity Test (eFAST) (Marino et al., 2008) was used to calculate the sensitivity of the model outputs to its inputs. The outputs and inputs of the analysis are the upstream reaction rates and the kinetic parameters, respectively. Briefly, eFAST is a variance-based sensitivity analysis that uses a variance decomposition method similar to ANOVA. The variance of an output is partitioned, and the algorithm determines what fraction of the variance can be explained by the variation in each input. The greater the output's variance is attributed to an input, the greater the input's influence is on the output. The first-order sensitivity index, S_i, measures the fraction of the model output's variance explained by the ith parameter's input variance:

$$S_i = \frac{\sigma_i^2}{\sigma_{total}^2}$$

To estimate the total-order sensitivity index, S_{Ti}, of a given parameter i, eFAST calculates the summed sensitivity index of the complementary set of parameters (i.e. all parameters except i). S_{Ti} is then calculated as the remaining variance excluding the contribution of the complementary set, S_{Ci}, as follows:

$$S_{Ti} = 1 - S_{Ci}$$

Thus, the S_{Ti} for a given input i measures how influential that input and all of its interactions are to a specific output. We selected to fit parameters with an $S_{Ti} \geq 0.5$ for all the model outputs. If both k_{on} and k_{off} for a single reaction were estimated to have an $S_{Ti} \geq 0.5$, then k_{on} was kept constant at 10^{-1} $(\mu M^{-1} \cdot s^{-1})$, as the association rate constant is reported to be fairly consistent across bimolecular reactions (Northrup and Erickson, 1992; Schlosshauer and Baker).

Parameter estimation

The values of the parameters shown to be influential based on the sensitivity analysis were estimated using Particle Swarm Optimization (PSO) (Kennedy, 2011; Shi, 2004; Venter and Sobieszczanski-Sobieski, 2003). This computational method estimates the parameter values by minimizing an objective function. Briefly, the algorithm works by having a population of candidate solutions (i.e., sets of parameter values) explore the defined parameter space or "search-space." Each candidate solution is guided by their own best-known position in the search-space based on the value of the objective function, as well as the entire set of candidate solutions' best-known positions. When improved positions are found, then these positions will guide the set of candidate solutions. This process is repeated until a satisfactory solution is discovered. Since the initial guesses (i.e., starting positions in the search-space) can influence the final result, we executed the algorithm 50 times using randomized initial guesses and report the median fitted values along with the standard deviation of the fits.

Estimation of goodness-of-fit

The search-space in PSO spanned ± 10-fold from baseline value for each estimated parameter. The predicted phosphorylated species values were processed in the same way as the experimental data (see above). That is, the reference time point for normalizing the predicted phosphorylated species values was the same time point used to normalize the corresponding experimental data points. The normalized phosphorylated species' levels predicted by the model were calibrated to the normalized signal intensity for the same phosphorylated species in the experimental data. The objective function for PSO was to minimize the sum of squared error (SSE) between the model and experimental values:

$$SSE = \sum_{j=1}^{k} \sum_{i=1}^{n} (\boldsymbol{E}_i - \boldsymbol{P}_i)^2$$

where $\boldsymbol{E}_i$ and $\boldsymbol{P}_i$ are the experimental and predicted values at the ith observation, respectively, and for the jth species, and n and k are the total number of experimental measurements and the total number of measured species, respectively. After 50 PSO runs, we further reduced the number of parameters to fit by using a Tukey's box-and-whiskers plot (Chambers et al., 1983) to see which parameters varied over one order of magnitude. The parameters that varied greatly were kept constant at their median values, and the parameters that varied within a tighter range were selected for the next round of fitting, as those parameters must be carefully specified in order to match experimental data.

Code availability

The full model is provided in Supplemental File S1, including the best-fit model parameter values.

Area under the curve

The area under the curve (AUC) was estimated using the MATLAB function *trapz*. This numerical integration method approximates the integration over an interval by partitioning the area into trapezoids.

Time to reach half-maximal concentration

The time to reach the species' half-maximal concentration ($t_{1/2}\,max$) was calculated by determining the time point where the phosphorylated species' concentration is half of its total concentration. Using vector notation, this is equivalent to

$$\frac{p\boldsymbol{X}_i}{p\boldsymbol{X}_i + \boldsymbol{X}_i} = \frac{1}{2}$$

where $p\boldsymbol{X} = \left[pX_1, \cdots, pX_n\right]^T$ and $\boldsymbol{X} = [X_1, \cdots, X_n]^T$ denote a column vector of a phosphorylated and dephosphorylated species' concentration over time, respectively, and i is the unit time step of n total time steps.

Signal duration

We define signal duration as the average time the rate of change of a phosphorylated species is positive. We follow the techniques described previously (Heinrich et al., 2002). Briefly, we define a function $\boldsymbol{f}(t)$ as

$$\boldsymbol{f} = \frac{d}{dt} p\boldsymbol{X}$$

and let $\boldsymbol{s}$ denote the subset of the time input, t, such that $\boldsymbol{f}(t) > 0$ for a given phosphorylated species ($p\boldsymbol{X}$):

$$\boldsymbol{s} = \{t \mid \boldsymbol{f}(t) > 0\}$$

Then, the signal duration ($\boldsymbol{\vartheta}$) for $\boldsymbol{f}$ is defined as

$$\boldsymbol{\vartheta} = 2\sigma$$

where σ is the standard deviation of $\boldsymbol{s}$. That is,

$$\sigma = \sqrt{\frac{\sum_{k=1}^{n} (\boldsymbol{s}_k - \mu)^2}{n - 1}}$$

where μ and n are the mean and length of $\boldsymbol{s}$, respectively.

Signal strength

We define the signal strength as the average intensity of the rate of change of a phosphorylated species during the same time interval as the signal duration. Let $\boldsymbol{B}$ denote the area under the curve of $\boldsymbol{f}(t)$ within the interval defined by $\boldsymbol{s}$:

$$\boldsymbol{B} = \int_{\boldsymbol{s}_1}^{\boldsymbol{s}_n} \boldsymbol{f}(t)dt$$

where the n is the final index of $\boldsymbol{s}$. We construct a rectangle whose area is equal to $\boldsymbol{B}$ with a corresponding width equal to $\boldsymbol{\vartheta}$. Then, the signal strength $(\boldsymbol{G})$ for $\boldsymbol{f}(t)$ is defined as

$$\boldsymbol{G} = \frac{\boldsymbol{B}}{\boldsymbol{\vartheta}}$$

where $\boldsymbol{G}$ is equivalent to the height of the rectangle. A geometric interpretation of signal duration $(\boldsymbol{\vartheta})$ and signal strength $(\boldsymbol{G})$ is illustrated in **Figure S6**.

Acknowledgments

We immensely appreciate the Finley group for critical evaluation of this manuscript as well as improvements with the model code. This work was supported a Viterbi/Graduate School Merit Fellowship (to S.Z.M).

References:

Altvater, B., Landmeier, S., Pscherer, S., Temme, J., Schweer, K., Kailayangiri, S., Campana, D., Juergens, H., Pule, M., and Rossig, C. (2009). 2B4 (CD244) Signaling by Recombinant Antigen-specific Chimeric Receptors Costimulates Natural Killer Cell Activation to Leukemia and Neuroblastoma Cells. Clin. Cancer Res. *15*, 4857–4866.

Aoukaty, A., and Tan, R. (2002). Association of the X-linked Lymphoproliferative Disease Gene Product SAP/SH2D1A with 2B4, a Natural Killer Cell-activating Molecule, Is Dependent on Phosphoinositide 3-Kinase. J. Biol. Chem. *277*, 13331–13337.

Araujo, R.P., Petricoin, E.F., and Liotta, L.A. (2005). A mathematical model of combination therapy using the EGFR signaling network. Biosystems *80*, 57–69.

Bar-Even, A., Noor, E., Savir, Y., Liebermeister, W., Davidi, D., Tawfik, D.S., and Milo, R. (2011). The Moderately Efficient Enzyme: Evolutionary and Physicochemical Trends Shaping Enzyme Parameters. Biochemistry (Mosc.) *50*, 4402–4410.

Baxter, A.G., and Hodgkin, P.D. (2002). Activation rules: the two-signal theories of immune activation. Nat. Rev. Immunol. *2*, 439–446.

Bellouquid, A., and CH-Chaoui, M. (2014). Asymptotic analysis of a nonlinear integro-differential system modeling the immune response. Comput. Math. Appl. *68*, 905–914.

Billadeau, D.D., Upshaw, J.L., Schoon, R.A., Dick, C.J., and Leibson, P.J. (2003). NKG2D-DAP10 triggers human NK cell–mediated killing via a Syk-independent regulatory pathway. Nat. Immunol. *4*, 557–564.

Bollino, D., and Webb, T.J. (2017). Chimeric antigen receptor–engineered natural killer and natural killer T cells for cancer immunotherapy. Transl. Res. *187*, 32–43.

Bryceson, Y.T., and Ljunggren, H.-G. (2011a). Natural Killer Cells: Biology, Physiology and Medicine – Part 1. J. Innate Immun. *3*, 213–215.

Bryceson, Y.T., and Ljunggren, H.-G. (2011b). Natural Killer Cells: Biology, Physiology and Medicine – Part 2. J. Innate Immun. *3*, 327–328.

Bubeník, J. (2003). Tumour MHC class I downregulation and immunotherapy (Review). Oncol. Rep. *10*, 2005–2008.

Chambers, J.M., Cleveland, W.S., Tukey, P.A., and Kleiner, B. (1983). Graphical Methods for Data Analysis (Belmont, Calif.□: Boston: Duxbury Press).

Chen, R., Relouzat, F., Roncagalli, R., Aoukaty, A., Tan, R., Latour, S., and Veillette, A. (2004). Molecular Dissection of 2B4 Signaling: Implications for Signal Transduction by SLAM-Related Receptors. Mol. Cell. Biol. *24*, 5144–5156.

Das, J. (2010). Activation or Tolerance of Natural Killer Cells Is Modulated by Ligand Quality in a Nonmonotonic Manner. Biophys. J. *99*, 2028–2037.

Disis, M.L., and Cheever, M.A. (1996). Oncogenic proteins as tumor antigens. Curr. Opin. Immunol. *8*, 637–642.

Dong, Z., Davidson, D., Pérez-Quintero, L.A., Kurosaki, T., Swat, W., and Veillette, A. (2012). The Adaptor SAP Controls NK Cell Activation by Regulating the Enzymes Vav-1 and SHIP-1 and by Enhancing Conjugates with Target Cells. Immunity *36*, 974–985.

Eftimie, R., Gillard, J.J., and Cantrell, D.A. (2016). Mathematical Models for Immunology: Current State of the Art and Future Research Directions. Bull. Math. Biol. *78*, 2091–2134.

Galandrini, R., Tassi, I., Mattia, G., Lenti, L., Piccoli, M., Frati, L., and Santoni, A. (2002). SH2-containing inositol phosphatase (SHIP-1) transiently translocates to raft domains and modulates CD16-mediated cytotoxicity in human NK cells. Blood *100*, 4581–4589.

Gattinoni, L., Jr, D.J.P., Rosenberg, S.A., and Restifo, N.P. (2006). Adoptive immunotherapy for cancer: building on success. Nat. Rev. Immunol. *6*, 383–393.

Gilfillan, S., Ho, E.L., Cella, M., Yokoyama, W.M., and Colonna, M. (2002). NKG2D recruits two distinct adapters to trigger NK cell activation and costimulation. Nat. Immunol. *3*, 1150–1155.

Giuriato, S., Payrastre, B., Drayer, A.L., Plantavid, M., Woscholski, R., Parker, P., Erneux, C., and Chap, H. (1997). Tyrosine Phosphorylation and Relocation of SHIP Are Integrin-mediated in Thrombin-stimulated Human Blood Platelets. J. Biol. Chem. *272*, 26857–26863.

Glienke, W., Esser, R., Priesner, C., Suerth, J.D., Schambach, A., Wels, W.S., Grez, M., Kloess, S., Arseniev, L., and Koehl, U. (2015). Advantages and applications of CAR-expressing natural killer cells. Front. Pharmacol. *6*.

Gridelli, C., Maione, P., Del Gaizo, F., Colantuoni, G., Guerriero, C., Ferrara, C., Nicolella, D., Comunale, D., De Vita, A., and Rossi, A. (2007). Sorafenib and sunitinib in the treatment of advanced non-small cell lung cancer. The Oncologist *12*, 191–200.

Guillerey, C., Huntington, N.D., and Smyth, M.J. (2016). Targeting natural killer cells in cancer immunotherapy. Nat. Immunol. *17*, 1025–1036.

Harris, L.A., Hogg, J.S., Tapia, J.-J., Sekar, J.A.P., Gupta, S., Korsunsky, I., Arora, A., Barua, D., Sheehan, R.P., and Faeder, J.R. (2016). BioNetGen 2.2: advances in rule-based modeling. Bioinformatics *32*, 3366–3368.

Heinrich, R., Neel, B.G., and Rapoport, T.A. (2002). Mathematical Models of Protein Kinase Signal Transduction. Mol. Cell *9*, 957–970.

Kennedy, J. (2011). Particle Swarm Optimization. In Encyclopedia of Machine Learning, (Springer, Boston, MA), pp. 760–766.

Kim, H.S., and Long, E.O. (2012). Complementary Phosphorylation Sites in the Adaptor Protein SLP-76 Promote Synergistic Activation of Natural Killer Cells. Sci. Signal. *5*, ra49–ra49.

Kim, H.S., Das, A., Gross, C.C., Bryceson, Y.T., and Long, E.O. (2010). Synergistic Signals for Natural Cytotoxicity Are Required to Overcome Inhibition by c-Cbl Ubiquitin Ligase. Immunity *32*, 175–186.

Kim, M.-S., Pinto, S.M., Getnet, D., Nirujogi, R.S., Manda, S.S., Chaerkady, R., Madugundu, A.K., Kelkar, D.S., Isserlin, R., Jain, S., et al. (2014). A draft map of the human proteome. Nature *509*, 575–581.

Klingemann, H.-G. (2005). Natural killer cell-based immunotherapeutic strategies. Cytotherapy *7*, 16–22.

Kwon, H.-J., and Kim, H.S. (2012). Signaling for Synergistic Activation of Natural Killer Cells. Immune Netw. *12*, 240.

Kwon, H.-J., Kwon, S.J., Lee, H., Park, H.-R., Choi, G.-E., Kang, S.-W., Kwon, S.W., Kim, N., Lee, S.Y., Ryu, S., et al. (2015). NK cell function triggered by multiple activating receptors is negatively regulated by glycogen synthase kinase-3β. Cell. Signal. *27*, 1731–1741.

Kwon, H.-J., Choi, G.-E., Ryu, S., Kwon, S.J., Kim, S.C., Booth, C., Nichols, K.E., and Kim, H.S. (2016). Stepwise phosphorylation of p65 promotes NF-κB activation and NK cell responses during target cell recognition. Nat. Commun. *7*, 11686.

Li, Y., Hermanson, D.L., Moriarity, B.S., and Kaufman, D.S. (2018). Human iPSC-Derived Natural Killer Cells Engineered with Chimeric Antigen Receptors Enhance Anti-tumor Activity. Cell Stem Cell.

Long, E.O., Sik Kim, H., Liu, D., Peterson, M.E., and Rajagopalan, S. (2013). Controlling Natural Killer Cell Responses: Integration of Signals for Activation and Inhibition. Annu. Rev. Immunol. *31*, 227–258.

Marino, S., Hogue, I.B., Ray, C.J., and Kirschner, D.E. (2008). A Methodology For Performing Global Uncertainty And Sensitivity Analysis In Systems Biology. J. Theor. Biol. *254*, 178–196.

Mellman, I., Coukos, G., and Dranoff, G. (2011). Cancer immunotherapy comes of age. Nature *480*, 480–489.

Mesecke, S., Urlaub, D., Busch, H., Eils, R., and Watzl, C. (2011). Integration of Activating and Inhibitory Receptor Signaling by Regulated Phosphorylation of Vav1 in Immune Cells. Sci. Signal. *4*, ra36–ra36.

Nanda, N.K., and Sercarz, E.E. (1995). Induction of anti-self-immunity to cure cancer. Cell *82*, 13–17.

Northrup, S.H., and Erickson, H.P. (1992). Kinetics of protein-protein association explained by Brownian dynamics computer simulation. Proc. Natl. Acad. Sci. *89*, 3338–3342.

Pappalardo, F., Palladini, A., Pennisi, M., Castiglione, F., and Motta, S. (2012). Mathematical and Computational Models in Tumor Immunology. Math. Model. Nat. Phenom. *7*, 186–203.

Pérez-Quintero, L.-A., Roncagalli, R., Guo, H., Latour, S., Davidson, D., and Veillette, A. (2014). EAT-2, a SAP-like adaptor, controls NK cell activation through phospholipase Cγ, Ca++, and Erk, leading to granule polarization. J. Exp. Med. *211*, 727–742.

Ramnath, N., Tan, D., Li, Q., Hylander, B.L., Bogner, P., Ryes, L., and Ferrone, S. (2006). Is downregulation of MHC class I antigen expression in human non-small cell lung cancer associated with prolonged survival? Cancer Immunol. Immunother. *55*, 891.

Romain, G., Senyukov, V., Rey-Villamizar, N., Merouane, A., Kelton, W., Liadi, I., Mahendra, A., Charab, W., Georgiou, G., Roysam, B., et al. (2014). Antibody Fc engineering improves frequency and promotes kinetic boosting of serial killing mediated by NK cells. Blood *124*, 3241–3249.

Romanski, A., Uherek, C., Bug, G., Seifried, E., Klingemann, H., Wels, W.S., Ottmann, O.G., and Tonn, T. (2016). CD19-CAR engineered NK-92 cells are sufficient to overcome NK cell resistance in B-cell malignancies. J. Cell. Mol. Med. *20*, 1287–1294.

Rosenberg, S.A., Yang, J.C., and Restifo, N.P. (2004). Cancer immunotherapy: moving beyond current vaccines. Nat. Med. *10*, 909–915.

Schlosshauer, M., and Baker, D. Realistic protein–protein association rates from a simple diffusional model neglecting long-range interactions, free energy barriers, and landscape ruggedness. Protein Sci. *13*, 1660–1669.

Shi, Y. (2004). Particle Swarm Optimization. 6.

Szewczuk, L.M., Tarrant, M.K., and Cole, P.A. (2009). Protein Phosphorylation by Semisynthesis: From Paper to Practice. Methods Enzymol. *462*, 1–24.

Theorell, J., Gustavsson, A.-L., Tesi, B., Sigmundsson, K., Ljunggren, H.-G., Lundbäck, T., and Bryceson, Y.T. (2014). Immunomodulatory activity of commonly used drugs on Fc-receptor-mediated human natural killer cell activation. Cancer Immunol. Immunother. *63*, 627–641.

Ting, A.T., Karnitz, L.M., and Schoon, R.A. (1992). Fc7 Receptor Activation Induces the Tyrosine Phosphorylation of Both Phospholipase C (PLC)-y1 and PLC-y2 in Natural Killer Cells. 5.

Venter, G., and Sobieszczanski-Sobieski, J. (2003). Particle Swarm Optimization. AIAA J. *41*, 1583–1589.

Zhou, C. (2012). Multi-targeted tyrosine kinase inhibitors for the treatment of non-small cell lung cancer: an era of individualized therapy. Transl. Lung Cancer Res. *1*, 72–77.

Supplemental Figure Legends

Figure S1. Results of eFAST sensitivity analysis. We performed a global sensitivity analysis to determine how sensitive the upstream reaction rates (44 outputs, horizontal-axis) are to variance in the kinetic parameters (138 inputs, vertical-axis). A total of 138 kinetics parameters (equally split into quadrants (A-D) for visualization) were varied. The color bar corresponds to the total FAST index, S_{Ti}, values. Parameters with an $S_{Ti} \geq 0.5$ were selected for fitting (56 in total), which can be identified in **Figure S2, A-B**.

Figure S2. Estimated parameter values. We estimated the kinetic parameter values using PSO. Fifty-six parameters were found to be influential to our model outputs via eFAST sensitivity analysis. These 56 parameters were varied from their baseline value $\pm$ 10-fold. The results are shown in panels A (28 parameters) and B (28 parameters). Results from the second and third iteration of fitting are shown in panels C and D, respectively. Points represent outliers according to Tukey's method.

Figure S3. Relationship between predicted absolute concentrations and signal intensity values. Since the molecular perturbation data includes only one or two data points, normalization according to the methods described above is not possible. Thus, we generated a standard curve between the predicted absolute concentration of a phosphorylated species ($p\boldsymbol{X}$) and its corresponding measured signal intensity (Q_{pX}) values at the discrete time points of experimental measurement. After model fitting, the signal intensity values of a species (horizontal axis) were plotted against the model's predicted absolute concentration of the same species (vertical axis). Using linear regression analysis in Prism (GraphPad), a mathematical relationship between signal intensity and species concentration was derived. Next, we used the equation to calculate the predicted absolute concentration from signal intensity data. These predicted concentration values were plotted as points in **Figure 3, E-H** and compared to the model simulations. We generated such figures and mathematical relationships for each panel in **Figure 3, E-H**. Here, we show the case for pSFK as an illustration. Circles: data points; dashed line: best-fit line.

Figure S4. Characteristic signaling differences when CD16 is reduced 100-fold. (A) Concentration profiles for activation-influencing species: pReceptor, pSFK, pErk, pAkt, and pPLCγ. (B) Magnitude of activation for the corresponding species in panel A via AUC analysis. (C) Time to reach half-maximal concentration for the corresponding species in panel A. Blue: CD16 pathway. Purple: 2B4 pathway. Orange: NKG2D pathway. Asterisks signify the highest AUC or lowest $t_{1/2}\ max$ based on *t*-test ($p < 0.001$).

Figure S5. Kinetic analysis of species activation when CD16 is reduced 100-fold. (A) Time derivatives of the concentration profiles for activation-influencing species: pReceptor, pSFK, pErk, pAkt, and pPLCγ. (B) The calculated signal duration for the corresponding species in panel A. (C) The signal strength for the corresponding species in panel A. Blue: CD16 pathway. Purple: 2B4 pathway. Orange: NKG2D pathway. Asterisks signify the highest signal duration or signal strength based on *t*-test ($p < 0.001$).

Figure S6. Signal duration and signal strength. The time derivative of a phosphorylated species, represented as $\boldsymbol{f}(t)$, plotted over time. The shaded area in the rectangle is equal to the shaded area under the curve. The height of the rectangle defines the curve's signal strength ($\boldsymbol{G}$) and the width of the rectangle defines the curve's signal duration ($\boldsymbol{\vartheta} = 2\sigma$).

Supplemental Files

File S1. Zipped file containing the computational models as a BioNetGen file and MATLAB .m files
File S2. Supplemental Figures
File S3. Supplemental Tables with model species and fitted parameter values

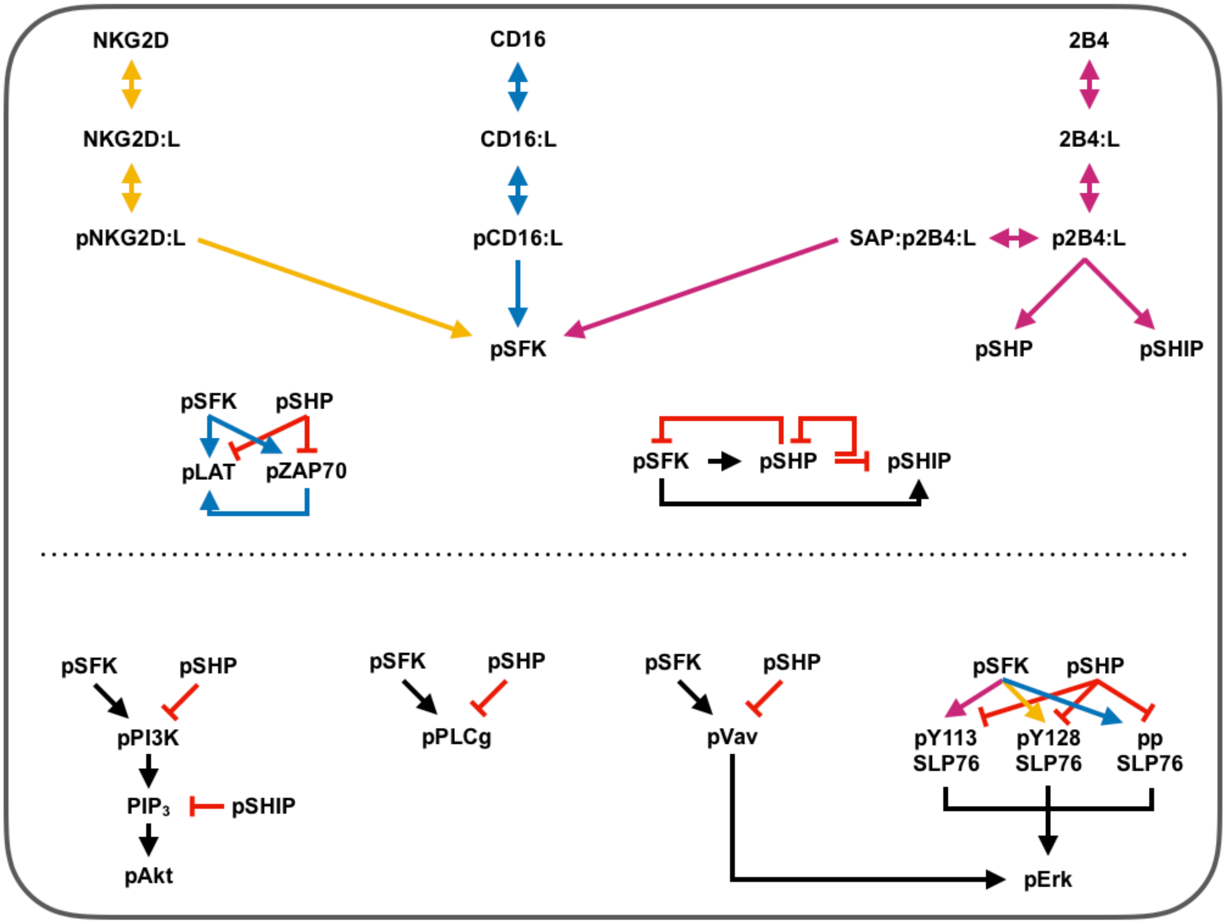
NKG2D
NKG2D:L
pNKG2D:L
CD16
CD16:L
pCD16:L
2B4
2B4:L
SAP:p2B4:L
p2B4:L
pSFK
pSHP
pSHIP
pSFK
pSHP
pLAT
pZAP70
pSFK
pSHP
pSHIP
pSFK
pSHP
pPI3K
PIP3
pSHIP
pAkt
pSFK
pSHP
pPLCg
pSFK
pSHP
pVav
pSFK
pSHP
pY113 SLP76
pY128 SLP76
pp SLP76
pErk

Figure 1. Model schematic. Reaction network for three stimulatory receptors expressed on the surface of NK cells: CD16, 2B4 and NKG2D. These receptors promote signaling species that mediate NK cell activation: SFK, Erk, Akt and PLCγ. Arrows indicate stimulation while red crossbars indicate inhibition. Orange arrows are specific to the NKG2D pathway; blue, CD16 pathway; purple, 2B4 pathway; black, all pathways. The dashed lines separate the upstream reactions from the downstream reactions.

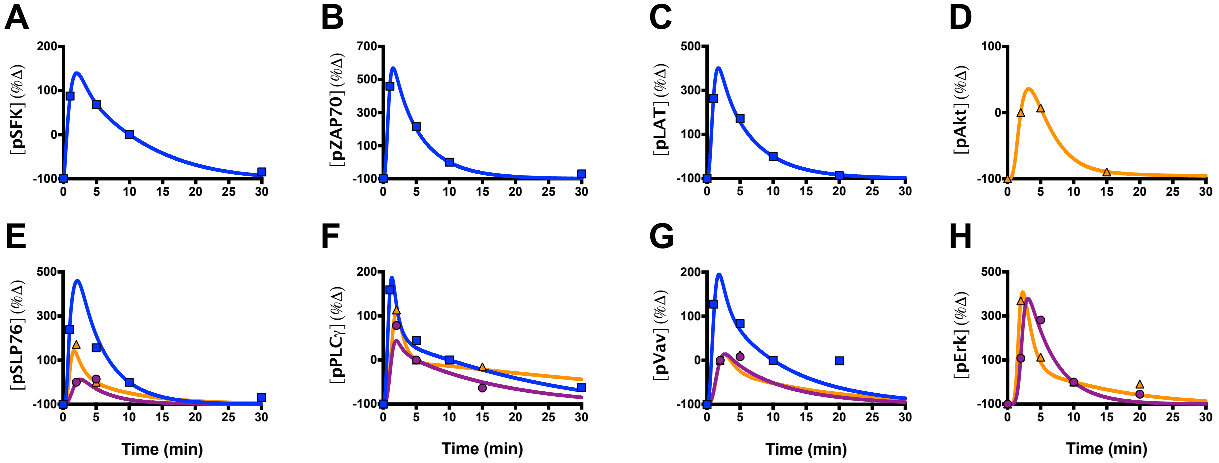

Figure 2. Model calibration. The model was fit to experimental data for (A) pSFK, (B) pZAP70, (C) pLAT, (D) pAkt, (E) pSLP76, (F) pPLCγ, (G) pVav and (H) pErk. Blue: CD16 pathway. Purple: 2B4 pathway. Orange: NKG2D pathway. Model predictions: solid lines. Experimental data: squares, CD16 stimulation; circles, 2B4 stimulation; triangles, NKG2D stimulation.

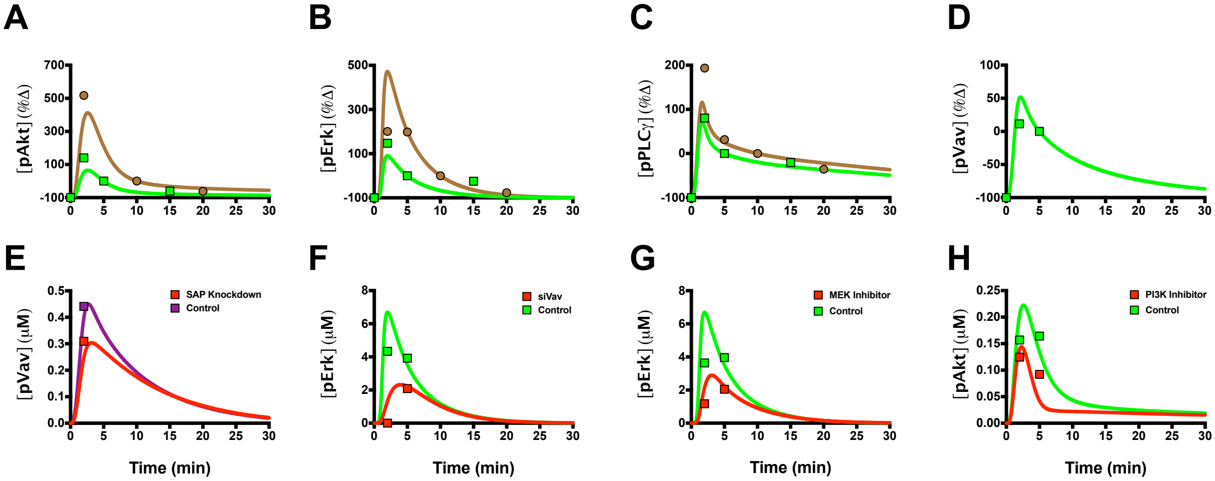

Figure 3. Model validation. The model was validated against separate experimental data, including the concentrations of: (A) pAkt, (B) pErk, (C) pPLC*γ* and (D) pVav over time via co-stimulation of 2B4 and NKG2D. The model was validated against data that incorporates signal-inhibiting perturbations: (E) pVav over time with SAP knockdown via 2B4 mono-stimulation, pErk over time with (F) siVav or (G) MEK inhibitor via 2B4 and NKG2D co-stimulation; (H) pAkt over time with PI3K inhibitor via 2B4 and NKG2D co-stimulation. Model predictions: solid lines. Experimental data: circles and squares. For (A) – (D), green and brown data indicate independent experimental studies.

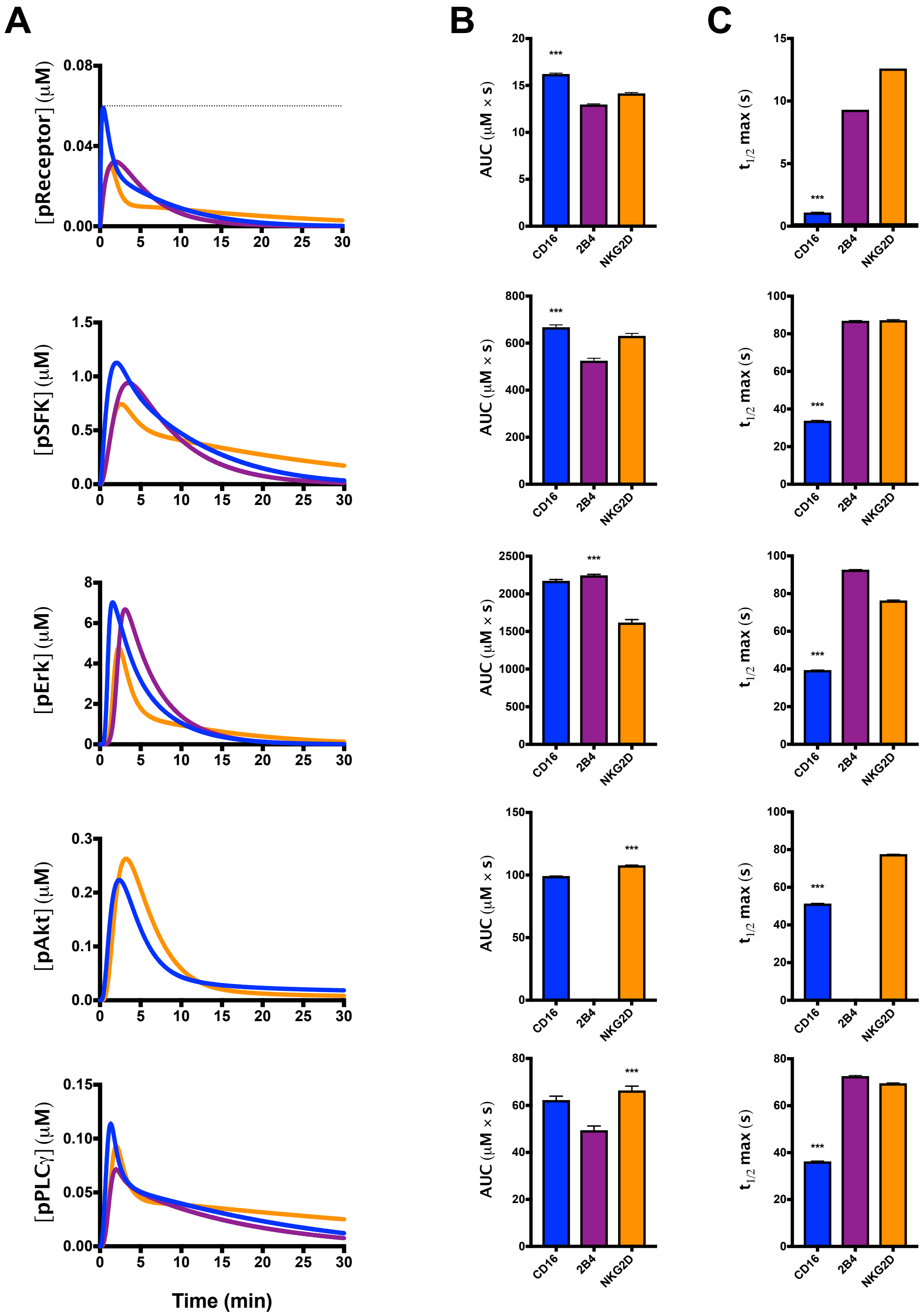

Figure 4. Characteristic signaling differences. (A) Concentration profiles for activation-influencing species: pReceptor, pSFK, pErk, pAkt, and pPLCγ. (B) Magnitude of activation for the corresponding species in panel A via AUC analysis. (C) Time to reach half-maximal concentration for the corresponding species in panel A. Blue: CD16 pathway. Purple: 2B4 pathway. Orange: NKG2D pathway. Asterisks signify the highest AUC or lowest $t_{1/2}\ max$ based on *t*-test ($p < 0.001$).

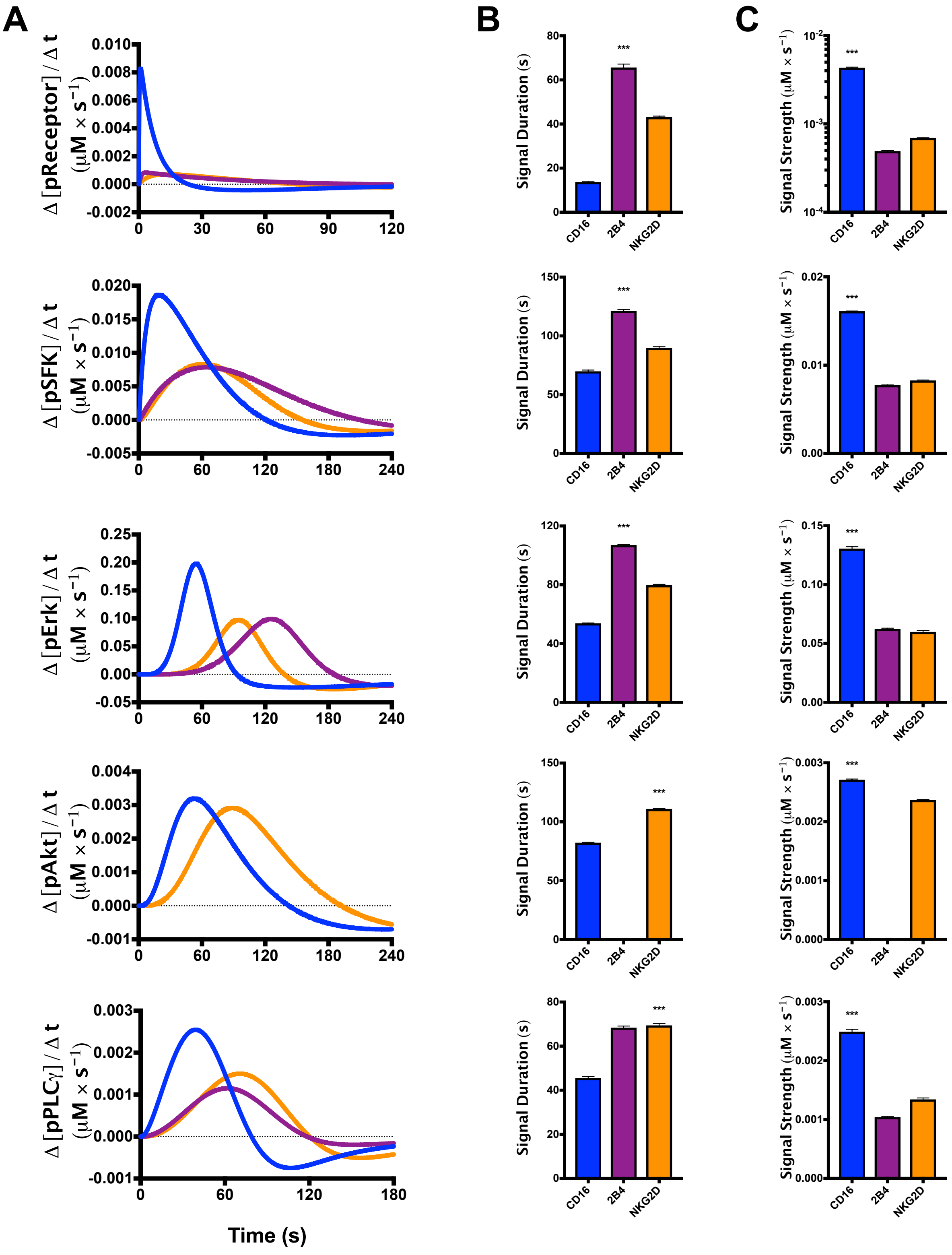

Figure 5. Kinetic analysis of species activation. (A) Time derivatives of the concentration profiles for activation-influencing species: pReceptor, pSFK, pErk, pAkt, and pPLCγ. (B) The calculated signal duration for the corresponding species in panel A. (C) The signal strength for the corresponding species in panel A. Blue: CD16 pathway. Purple: 2B4 pathway. Orange: NKG2D pathway. Asterisks signify the highest signal duration or signal strength based on *t*-test $(p < 0.001)$.

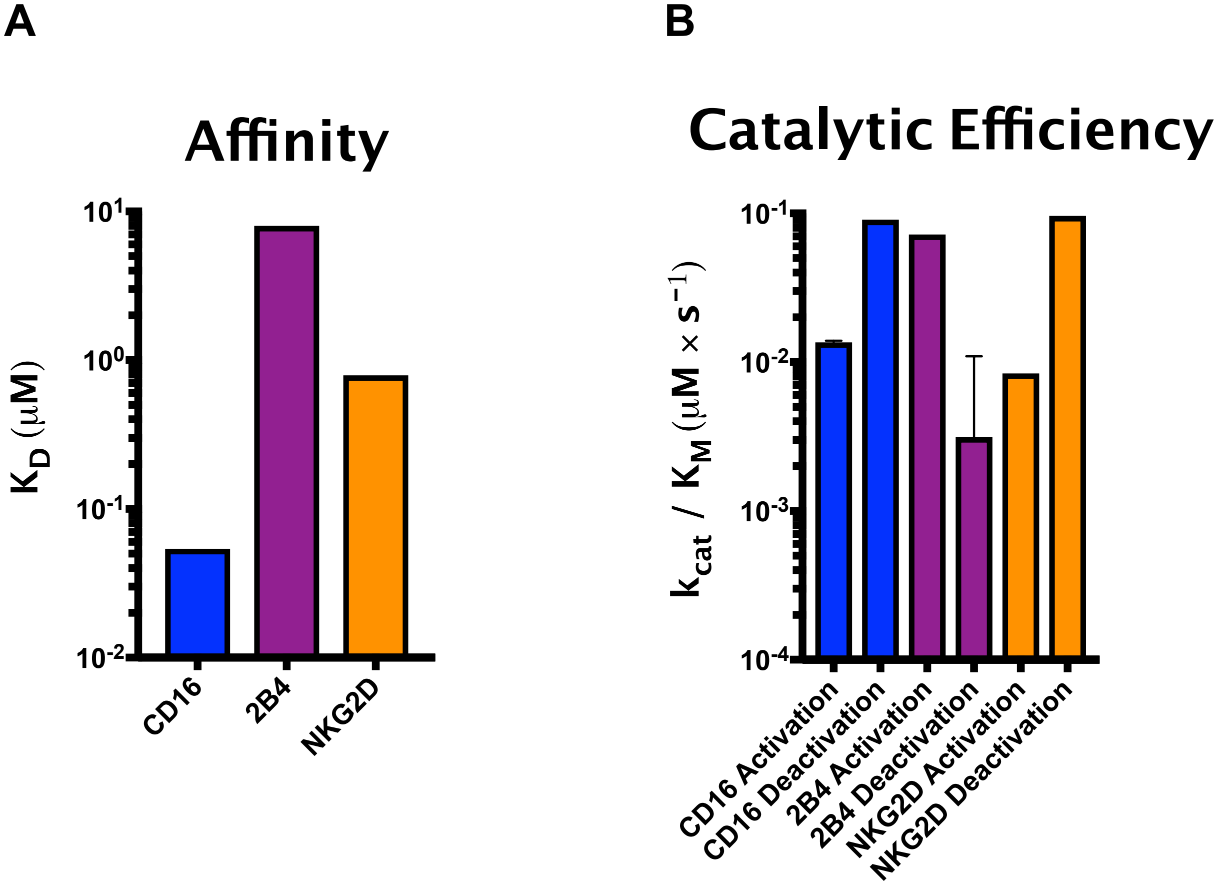

Figure 6. Comparison of estimated parameter values for pathway activation. (A) The estimated dissociation constant (K_D) between each receptor and its ligand, and (B) catalytic efficiency $(\frac{k_{cat}}{K_M})$ for receptor activation and deactivation. Blue: CD16 pathway. Purple: 2B4 pathway. Orange: NKG2D pathway.

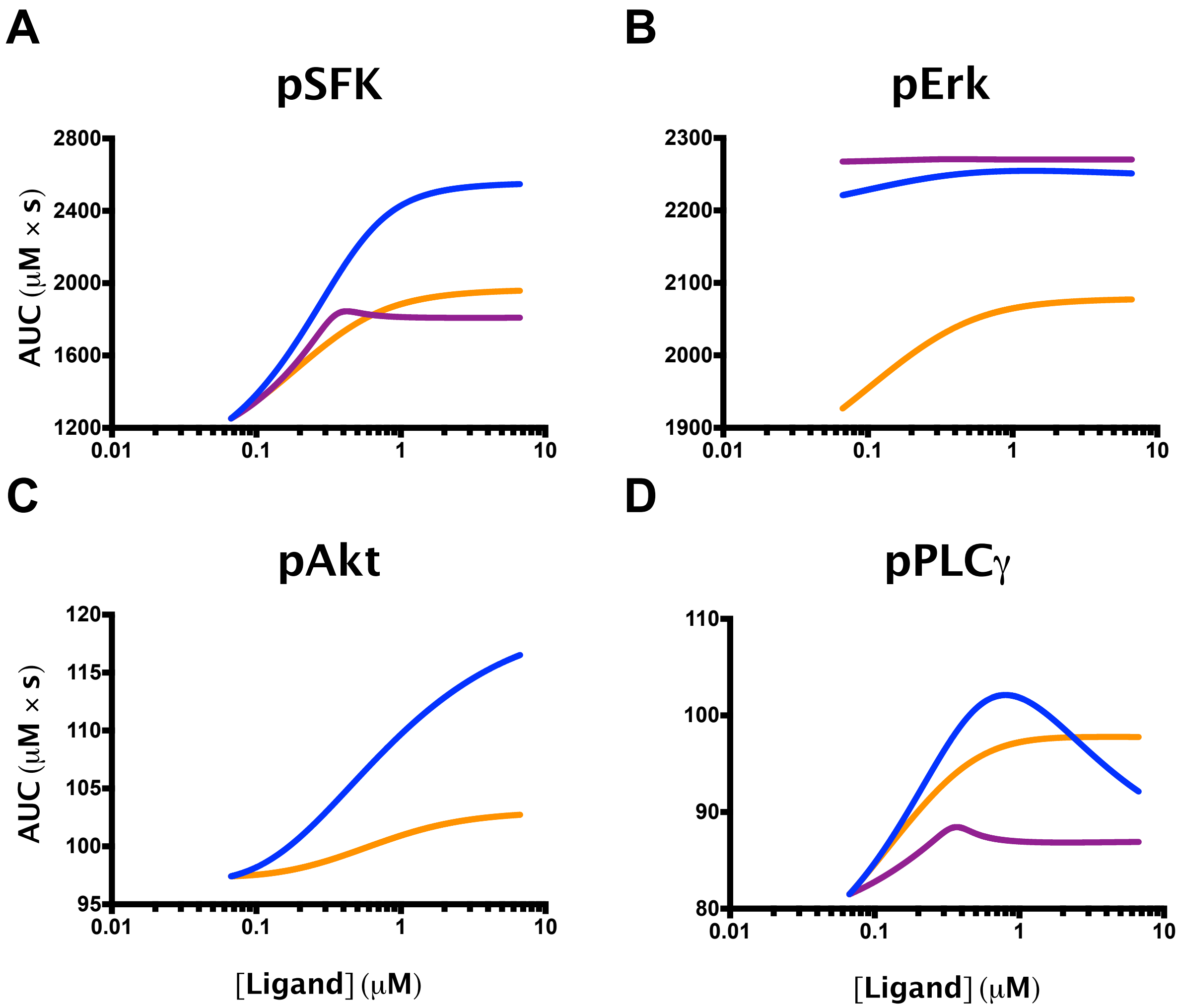

Figure 7. Mono-stimulation of receptors with various ligand concentrations. The AUC of (A) pSFK, (B) pErk, (C) pAkt and (D) pPLCγ was calculated after 30 minutes of ligand stimulation. For each panel, the ligand concentrations were varied by two orders of magnitude from baseline $(6.67 \times 10^{-2} \mu M)$. Blue, mono-stimulation of CD16; Purple, mono-stimulation of 2B4; Orange, mono-stimulation of NKG2D.

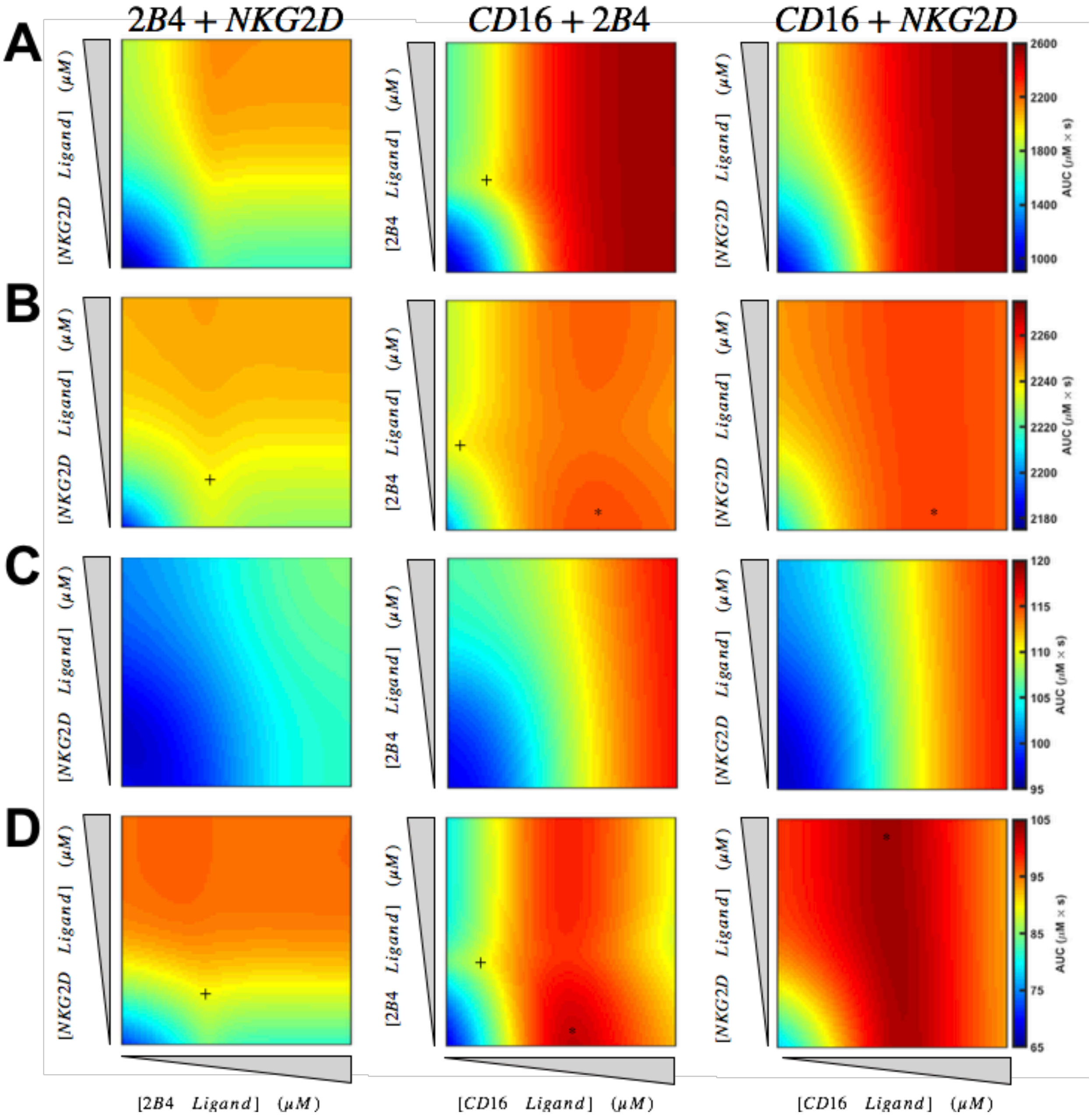

Figure 8. Pairwise stimulation of receptors with various ligand concentrations. The AUC of (A) pSFK, (B) pErk, (C) pAkt and (D) pPLCγ as a function of ligand concentration. For each panel, the concentration of ligands was varied by two orders of magnitude from baseline $(6.67 \times 10^{-2} \mu M)$. Left column, co-stimulation of 2B4 and NKG2D; middle column, co-stimulation of CD16 and 2B4; right column, co-stimulation of CD16 and NKG2D.